Nonreciprocal Components Based on Switched Transmission Lines

Aravind Nagulu⬮, *Student Member, IEEE*, Tolga Dinc⬮, *Student Member, IEEE*, Zhicheng Xiao,
Mykhailo Tymchenko, Dimitrios L. Sounas, *Senior Member, IEEE*, Andrea Alù⬮, *Fellow, IEEE*,
and Harish Krishnaswamy⬮, *Member, IEEE*

Abstract—Nonreciprocal components, such as isolators and circulators, are critical to wireless communication and radar applications. Traditionally, nonreciprocal components have been implemented using ferrite materials, which exhibit nonreciprocity under the influence of an external magnetic field. However, ferrite materials cannot be integrated into IC fabrication processes and, consequently, are bulky and expensive. In the recent past, there has been strong interest in achieving nonreciprocity in a nonmagnetic IC-compatible fashion using spatio-temporal modulation. In this paper, we present a general approach to nonreciprocity based on switched transmission lines. Switched transmission lines enable broadband, lossless, and compact nonreciprocity and a wide range of nonreciprocal functionalities, including nonreciprocal phase shifters, ultra-broadband gyrators and isolators, frequency-conversion isolators, and high-linearity/high-frequency/ultra-broadband circulators. We present a detailed theoretical analysis of the various nonidealities that impact insertion loss and provide design guidelines. The theory is validated by experimental results from discrete-component-based gyrators and isolators and a 25-GHz circulator fabricated in a 45-nm SOI CMOS technology.

Index Terms—Circulators, CMOS, full duplex, gyrators, isolators, linear periodically time-varying (LPTV) circuits, millimeter-wave passive components, nonreciprocity, radars, ultra-wideband (UWB) communication, UWB circuit techniques.

I. INTRODUCTION

NONRECIPROCAL components, such as gyrators, isolators, and circulators, have numerous applications in the fields of wireless communication and radar. Frequency-modulated continuous-wave (FMCW) radars typically operate in simultaneous-transmit-and-receive (STAR) mode, and

a circulator is critical to enable the transmitter and the receiver to share the same antenna and avoid saturation of the receiver. Full-duplex wireless is an emerging wireless communication paradigm, which has drawn significant research interest in recent years [1]–[10] due to its potential to double the spectral efficiency in the physical layer and offer numerous other benefits in higher layers. Unlike traditionally used time-division or frequency-division duplexing schemes, in full-duplex wireless, the transmitter and the receiver *operate at the same time and at the same frequency*. Once again, the circulator is critical in allowing the transmitter and the receiver to share the same antenna. Isolators are commonly used to protect power amplifiers from reflections at the antenna interface. The gyrator was postulated by Tellegen [11] as the fifth linear circuit element after the resistor, capacitor, inductor, and transformer, providing a nonreciprocal phase equal to π, and is a basic nonreciprocal element, which can be used to realize arbitrary passive nonreciprocal circuits [12], [13].

Lorentz reciprocity states that any linear and time-invariant (LTI) medium with symmetric permittivity and permeability tensors is reciprocal. Historically, reciprocity has been broken by biasing magnetic (ferrite) materials using permanent magnets [14], [15]. However, magnetic materials are incompatible with IC fabrication technology, and therefore, magnetic nonreciprocal components tend to be bulky and expensive. IC-compatible circulators have been proposed using the inherent nonreciprocal behavior of active voltage-/current-biased transistors [16]–[19]. However, active nonreciprocal components are severely limited by the linearity and noise performance of the active transistors and are therefore not suitable for wireless applications which demand stringent performance on those fronts [20]. Nonlinearity can be used to violate reciprocity and has been extensively studied in the optical domain [21]–[24], but these techniques have limited utility in wireless communication applications due to their stringent linearity constraints.

Recently, exciting research efforts have been made to break reciprocity using spatio-temporal modulation [25]–[28], with permittivity being the material parameter that is modulated. In [25], a transmission line is periodically loaded with varactors, and a traveling-wave modulates the varactors along the line. The unidirectional modulation signal imparts a direction-dependent frequency conversion to the input signal as it travels along the line. Thus, forward and reverse traveling signals are

separated in frequency and can be isolated from each other using a frequency diplexer. In this structure, the length of the transmission line required is inversely proportional to the modulation contrast. In general, however, permittivity modulation is weak, with varactors exhibiting a typical C_{max}/C_{min} ratio of 2–4 on chip. As a result, a large form-factor is required to achieve strong nonreciprocity. Furthermore, varactors exhibit very poor quality factor as the operation frequency is increased to millimeter-wave frequencies, resulting in higher insertion loss. In [26] and [27], it was demonstrated that traveling-wave modulation in a resonant ring results in angular momentum biasing and strong nonreciprocity without frequency conversion. The ring can be miniaturized using lumped components, but this degrades the operating bandwidth. Most importantly, as before, the limitations of permittivity modulation using varactors, namely limited modulation contrast and the degradation of the quality factor as frequency increases, remain the same.

On the other hand, conductivity can be very efficiently and strongly modulated in semiconductor media, with CMOS transistors exhibiting ON/OFF conductance ratios as high as 10^3–10^5 [29]. It has been shown that by modulating the conductivity, i.e., switching transistors, on either side of a delay medium, extremely strong, low-loss, and broadband nonreciprocity can be achieved within a small form-factor [30]–[36]. The first demonstration involved staggered (i.e., phase-shifted) switching of transistors across a capacitor bank (commonly called an N-path filter [37], [38]) [30]. The phase-shifted N-path filter realizes an electrically infinitesimal gyrator, which was then embedded within a ring to realize a compact circulator. The placement within the ring was further optimized to suppress the voltage swing at the gyrator for transmitter-port excitations, enhancing the linearity and power handling. However, this approach suffers from low bandwidth because the capacitors do not provide a true time delay. In addition to this, N-path filters are not realizable at millimeter-wave frequencies due to their stringent clocking requirements as they require multiple phases of a clock at the frequency of operation. When the delay medium is replaced by a transmission line of appropriate length, nonreciprocity can be observed over much wider bandwidths. In addition to this, the modulation frequency can be greatly reduced relative to the operating frequency [31], [32]. These concepts were leveraged to realize the first millimeter-wave (25 GHz) passive nonmagnetic circulator in a CMOS technology in [31] and [32]. Reference [36] is a review of the N-path-filter-based circulator [30] and the millimeter-wave circulator [32]. Similar concepts were used in [33] to demonstrate an ultra-broadband circulator operating from 200 kHz to 200 MHz using discrete switches and coaxial cable delays and in [34] to implement a 0.2-μm GaN HEMT MMIC circulator operating up to 1 GHz.

This paper presents an exhaustive set of various nonreciprocal structures possible by using spatio-temporal conductivity modulation across transmission line delays, including an arbitrary phase-nonreciprocal element, an ultra-broadband gyrator, a frequency-conversion isolator, an ultra-broadband isolator, and ultra-broadband/high-linearity/high-frequency circulators. A detailed analysis for estimating the transmission
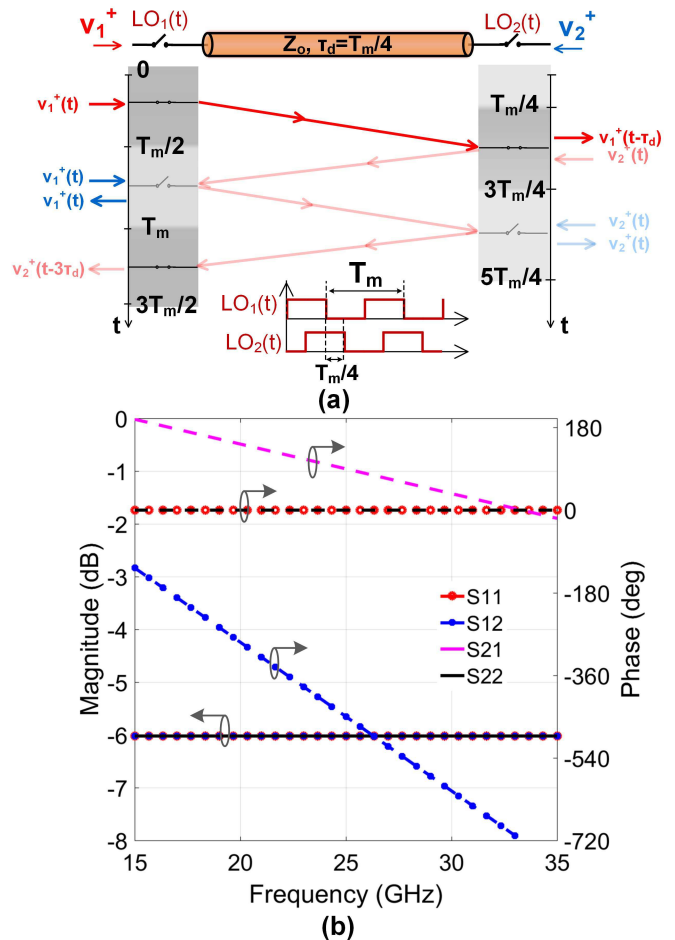

Fig. 1. Single-ended phase-nonreciprocal element (a) circuit diagram and operation and (b) fundamental-to-fundamental scattering parameters for $f_m = 8.33$ GHz.

losses is presented, along with results from a 25-GHz 45-nm SOI CMOS circulator prototype as a case study. This analysis can aid in choosing between different implementation technologies, fabrication processes, and nonreciprocal element topologies, and in performance optimization during the design phase. The rest of this paper is organized as follows. Section II discusses various phase-nonreciprocal configurations. Section III discusses various isolator and circulator topologies. Section IV contains a detailed analysis for estimating losses. Section V considers case studies implemented using discrete switches and coaxial cables, while Section VI details the 25-GHz 45-nm SOI CMOS circulator case study. Section VII concludes this paper.

II. PHASE NONRECIPROCITY

A. Single-Ended Phase-Nonreciprocal Element

Fig. 1(a) shows the circuit diagram and the operation of a single-ended phase-nonreciprocal element. It consists of a transmission-line segment whose characteristic impedance is equal to the port impedance and is sandwiched between two switches which are modulated using signals $LO_1(t)$ and $LO_2(t)$. The switches toggle between zero resistance (ON state) and infinite resistance (OFF state) when their

This article has been accepted for inclusion in a future issue of this journal. Content is final as presented, with the exception of pagination.

NAGULU *et al.*: NONRECIPROCAL COMPONENTS BASED ON SWITCHED TRANSMISSION LINES

3

modulation signals change between high and low values (1 and 0), respectively. The modulation signals $LO_1(t)$ and $LO_2(t)$ are 50% duty cycle square-wave signals with a period of T_m. The modulation signal of the right-hand side switch $LO_2(t)$ is delayed with respect to that of the left-hand side switch $LO_1(t)$ by $T_m/4$, which is also the propagation delay of the transmission line.

The operation of this structure can be explained using the time-domain analysis. For signals traveling from left to right, any arbitrary signal incident at port 1 when $LO_1(t)$ is high will be transmitted to port 2 in one pass, experiencing a delay of $T_m/4$, because the propagation delay of the transmission line is equal to the delay between the modulation signals. The signal incident at port 1 gets reflected when $LO_1(t)$ is low. However, for signals traveling from right to left, the signal incident at port 2 when $LO_2(t)$ is high will be transmitted to port 1 after three passes, experiencing a delay of $3T_m/4$, because at the end of the first two passes, the signal sees an open termination due to an OFF-state switch and experiences a total reflection. When $LO_2(t)$ is low, the signal incident at port 2 gets reflected. As a result of the additional reflections for incident signals from port 2 compared with port 1, the structure exhibits a different phase response for the signals traveling from left to right and right to left, making the structure nonreciprocal in phase. The behavior of the structure can be expressed in the time domain as

$$v_1^-(t) = v_1^+(t)(1 - LO_1(t)) + v_2^+\left(t - \frac{3T_m}{4}\right) LO_2\left(t - \frac{3T_m}{4}\right) \quad (1)$$

$$v_2^-(t) = v_1^+\left(t - \frac{T_m}{4}\right) LO_1\left(t - \frac{T_m}{4}\right) + v_2^+(t)(1 - LO_2(t)). \quad (2)$$

In general, linear periodically time-varying (LPTV) circuits are represented using harmonic transfer functions, which capture frequency conversion effects [39], [40]. For simplicity, here, we only show the fundamental-to-fundamental S-parameter matrix by taking the Fourier transform of the time-domain equations

$$S = \begin{pmatrix} \dfrac{1}{2} & \dfrac{1}{2}e^{-j\omega\frac{3T_m}{4}} \\ \dfrac{1}{2}e^{-j\omega\frac{T_m}{4}} & \dfrac{1}{2} \end{pmatrix}. \quad (3)$$

One-fourth of the power incident into the port is transmitted to the other port, one-fourth of the power is reflected due to the fact that the switch is open for 50% of time, i.e., infinite impedance mismatch, and the remaining half is converted to other frequencies (i.e., intermodulation products) due to the switching action. Fig. 1(b) shows the fundamental-to-fundamental S-parameters around 25 GHz for $f_m = 8.33$ GHz.

B. Balanced Configuration: Arbitrary Phase-Nonreciprocal Element

Harmonic conversion and the effect of infinite impedance mismatch of the single-ended phase-nonreciprocal element can be easily overcome by adding another parallel branch switched with complementary clocks $\overline{LO_1}(t)$ and $\overline{LO_2}(t)$, as shown in Fig. 2(a). The incident signal at port 1 (port 2) travels
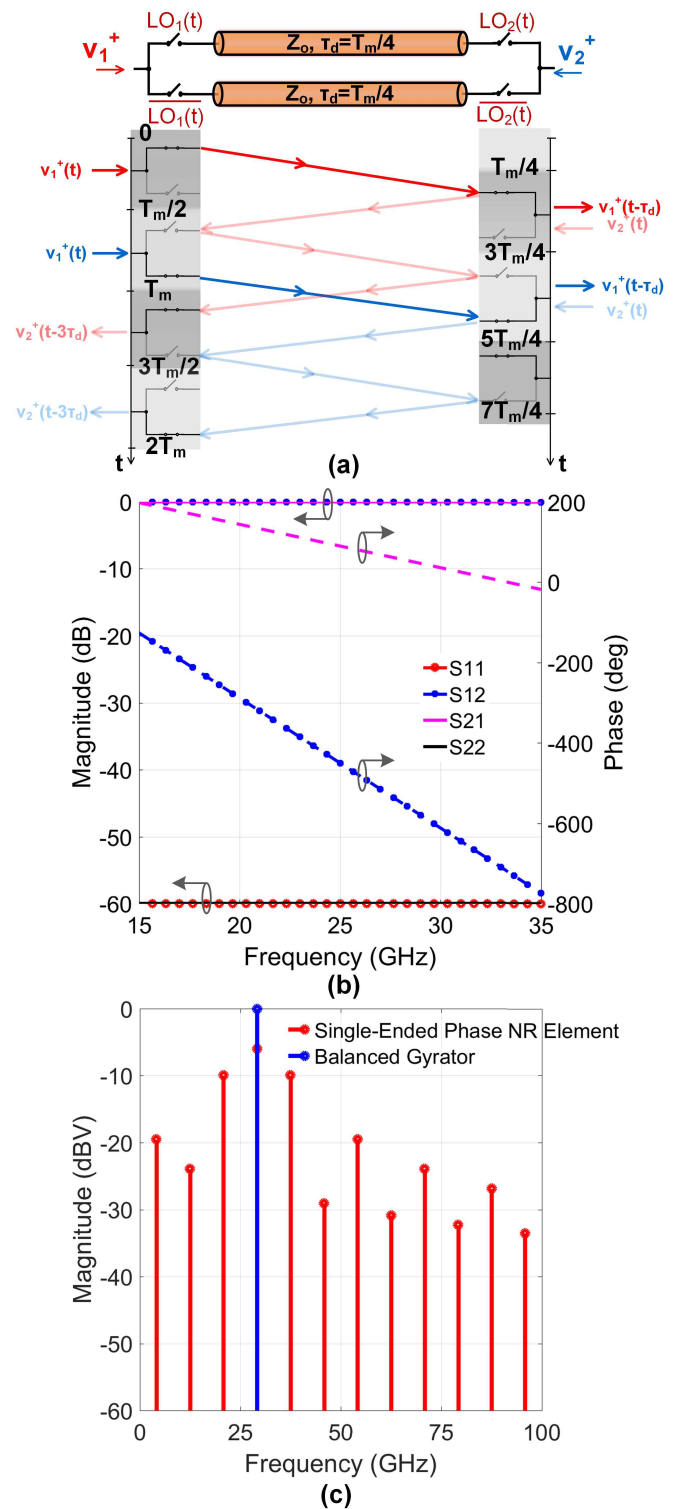

Fig. 2. Balanced arbitrary phase-nonreciprocal element (a) circuit diagram and operation, (b) scattering parameters for $f_m = 8.33$ GHz, and (c) voltage spectrum at port 2, when the 1-V, 29.16-GHz signal is incident at port 1 of the single-ended phase nonreciprocal element modulated and the balanced gyrator at 8.33 GHz.

through the first transmission line when $LO_1(t)$ ($LO_2(t)$) is high, and the second when $LO_1(t)$ ($LO_2(t)$) is low, making the structure completely matched with lossless transmission. The behavior of the structure can be expressed in the time

This article has been accepted for inclusion in a future issue of this journal. Content is final as presented, with the exception of pagination.

4

IEEE TRANSACTIONS ON MICROWAVE THEORY AND TECHNIQUES

domain as

$$v_1^-(t) = v_2^+\left(t - \frac{3T_m}{4}\right) \qquad (4)$$

$$v_2^-(t) = v_1^+\left(t - \frac{T_m}{4}\right). \qquad (5)$$

By taking Fourier transform of the time-domain equations, the S-parameter matrix can be calculated as

$$S = \begin{pmatrix} 0 & e^{-j\omega\frac{3T_m}{4}} \\ e^{-j\omega\frac{T_m}{4}} & 0 \end{pmatrix}. \qquad (6)$$

Interestingly, in this balanced configuration, intermodulation products generated in the first path and the second path will have opposite phase and cancel each other. Therefore, while the structure is internally LPTV, at its ports, it features no frequency conversion and appears LTI. Fig. 2(c) shows the voltage spectrum at port 2 when port 1 of the balanced configuration and the single-ended phase nonreciprocal element (both modulated at 8.33 GHz) are excited with a 1-V, 29.16-GHz signal. For the single-ended structure, several intermodulation products are created, and magnitude at the signal frequency is 6 dB lower, which is consistent with (3). However, in the balanced configuration, due to cancellation from the first and second paths, no intermodulation products are generated, and the signal is transmitted without any transmission loss.

At the odd multiples of the modulation frequency, $\omega = (2n+1)\omega_m$, where $\omega_m = 2\pi/T_m$ and, $n = 0, 1, 2, 3\ldots$, the phases from left to right and right to left are $-(2n+1)\pi/2$ and $-3(2n+1)\pi/2$, respectively. In this case, the structure behaves as a gyrator, providing a nonreciprocal phase equal to π [11]. Fig. 2(b) shows the S-parameters around a gyration frequency of 25 GHz for $f_m = 8.33$ GHz. In addition to this, at any given input frequency, a value of the modulation frequency ω_m can be chosen to realize a nonreciprocal phase difference of arbitrary value $\Delta\Phi = \pi(\omega/\omega_m)$. Of course, reconfiguring the value of this nonreciprocal phase shift after implementation requires reconfiguring the transmission line so that its delay matches the modulation frequency change.

While ideally lossless, in practice, the transmission loss will be limited by the quality factor and bandwidth of the transmission line and nonzero switch resistance. A limited bandwidth of the transmission line will allow transmission of only a limited number of harmonics and therefore imperfect reconstruction of the signal at the output port. The bandwidth of operation will be limited by the dispersion characteristics of the transmission line, switch parasitic capacitance, and rise/fall time of the modulation clocks. In the presence of a finite quality factor in the transmission lines, signals incident at port 2 experience more loss because they get transmitted after three passes when compared with the signals incident at port 1 which get transmitted after one pass.

C. Doubly Balanced Configuration: Ultra-Broadband Gyrator

Even though the balanced structure provides nonreciprocal phase response over an infinite bandwidth, it behaves as a gyrator only at discrete frequencies. In addition to this,
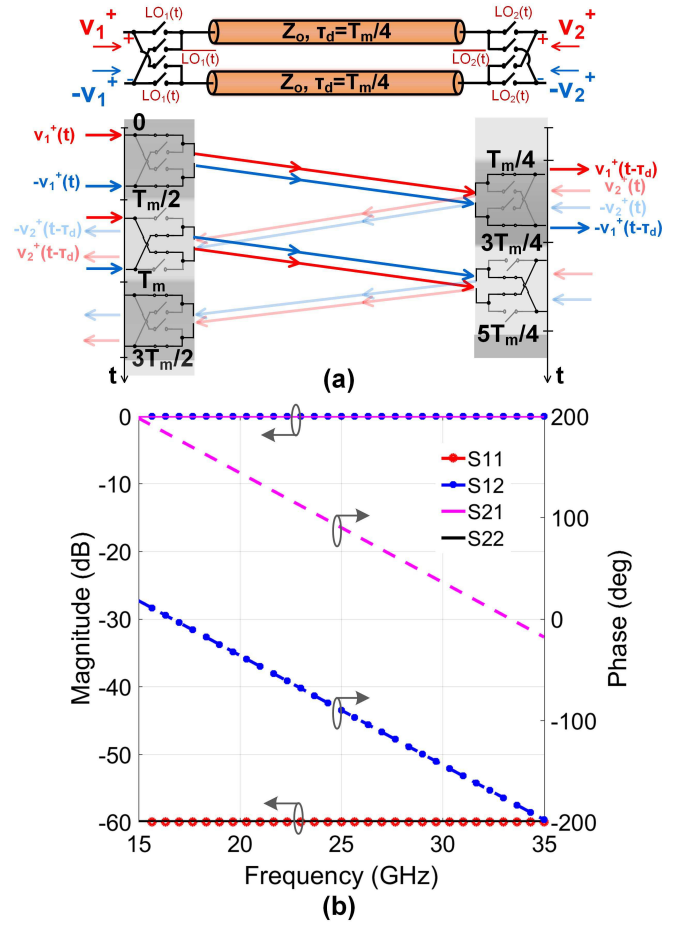

Fig. 3. Doubly balanced ultra-broadband gyrator (a) circuit diagram and operation and (b) scattering parameters for $f_m = 8.33$ GHz.

in a practical implementation, the transmission loss in forward and reverse directions will be imbalanced. Another interesting variant is a doubly balanced nonreciprocal element, as shown in Fig. 3(a), which exploits differential signaling for both the modulation signal as well as the input signal. It consists of a differential transmission line, with a characteristic impedance equal to the differential port impedance, which is sandwiched between two doubly balanced switch sets (often called Gilbert-quad mixers). A Gilbert-quad switch set consists of four switches where two switches connect the input and output directly when the modulation signal is high and the other two switches (crisscrossed) swap the signal polarity when the modulation signal is low. The switch sets on the left and right of the transmission line are driven by the modulation signals $LO_1(t)$ and $LO_2(t)$, respectively. Similar to the balanced case, the modulation signal of the right-hand side switch $LO_2(t)$ is delayed with respect to that of the left-hand side switch $LO_1(t)$ by a value $T_m/4$, which is also the propagation delay of the transmission line.

In this configuration, signals traveling from left to right, incident at port 1, get transmitted to port 2 without any sign inversion in the first half cycle and with two sign inversions that cancel each other in the second half cycle. On the other hand, signals traveling from right to left, incident at port 2, get

transmitted to port 1 with a sign inversion from the left-hand side mixer in the first half cycle and a sign inversion from the right-hand side mixer in the second half cycle. The behavior of the structure can be expressed in the time domain as shown in the following:

$$v_1^-(t) = m(t) \times v_2^+\left(t - \frac{T_m}{4}\right)$$
$$\times m\left(t - \frac{T_m}{2}\right)$$
$$= -v_2^+\left(t - \frac{T_m}{4}\right) \qquad (7)$$

$$v_2^-(t) = m\left(t - \frac{T_m}{4}\right) \times v_1^+\left(t - \frac{T_m}{4}\right)$$
$$\times m\left(t - \frac{T_m}{4}\right)$$
$$= v_1^+\left(t - \frac{T_m}{4}\right) \qquad (8)$$

where $m(t)$ is the multiplication factor due to the switching action of a quad-mixer, which is a square-wave signal between $+1$ and -1 with 50% duty cycle and period of T_m. By taking Fourier transform of the time-domain equations, the S-parameter matrix can be calculated as

$$S = \begin{pmatrix} 0 & -e^{-j\omega\frac{T_m}{4}} \\ +e^{-j\omega\frac{T_m}{4}} & 0 \end{pmatrix}. \qquad (9)$$

As expected, this doubly balanced structure also appears LTI externally while being internally LPTV. Most importantly, this structure describes an ideal gyrator over an infinite bandwidth. Fig. 3(b) shows the S-parameters around 25 GHz for $f_m = 8.33$ GHz. Ideally, zero insertion loss and a perfect non-reciprocal phase shift of π are possible over infinite bandwidth at arbitrarily small sizes through appropriate increase of the modulation frequency. In practice, transmission losses will be limited by the quality factor and bandwidth of the transmission lines and nonzero switch resistance. The bandwidth of operation by the dispersion characteristics of the transmission line, switch parasitic capacitance, and rise/fall time of the modulation clock and the size by the practicalities of switching solid state switches at increasing modulation frequency and the associated power consumption. It should also be mentioned that in the presence of losses, this structure continues to behave as a perfect gyrator with symmetric losses because the phase nonreciprocity is achieved due to sign inversion as opposed to path length differences.

D. Frequency-Domain Analysis of the Ultra-broadband Gyrator

The ultra-broadband gyrator can be interpreted as a transmission line sandwiched between two mixers and can be analyzed in the frequency domain. The multiplication factors of the left-hand side mixer and the right-hand side mixer, $m(t)$ and $m(t - (T_m/4))$, can be expressed in the frequency domain as shown in the following:

$$m(t) = \frac{2}{j\pi}\sum_{n=1}^{\infty}\frac{1}{2n-1}(e^{j(2n-1)\omega_m t} - e^{-j(2n-1)\omega_m t}) \qquad (10)$$

$$m\left(t - \frac{T_m}{4}\right) = \frac{2}{j\pi}\sum_{n=1}^{\infty}\frac{1}{2n-1}(e^{-j\frac{(2n-1)\pi}{2}}e^{j(2n-1)\omega_m t}$$
$$- e^{j\frac{(2n-1)\pi}{2}}e^{-j(2n-1)\omega_m t}). \qquad (11)$$

An input signal, $e^{j\omega t}$ traveling from left to right, after passing through the left-hand side mixer, will be multiplied with the multiplication factor $m(t)$, resulting in the following:

$$v_1^+(t) \times m(t) = \frac{2}{j\pi}\sum_{n=1}^{\infty}\frac{1}{2n-1}(e^{j(\omega+(2n-1)\omega_m)t}$$
$$- e^{j(\omega-(2n-1)\omega_m)t}). \qquad (12)$$

From this equation, we can see that the transmission line supports signals at infinitely many intermodulation frequencies, and therefore, dispersion-free operation of the line is critical. As can be seen, the amplitude of higher order intermodulation products becomes progressively smaller, and therefore, dispersion at frequencies further away from the operation frequency will have a progressively smaller effect. A quantification of the impact of transmission-line dispersion is given in Section IV. This signal experiences a delay of $T_m/4$ through the transmission line at which point it can be expressed as shown in the following:

$$v_1^+\left(t - \frac{T_m}{4}\right) \times m\left(t - \frac{T_m}{4}\right)$$
$$= \frac{2}{j\pi}e^{-j\omega\frac{T_m}{4}}\sum_{n=1}^{\infty}\frac{1}{2n-1}\left(e^{-j\frac{(2n-1)\pi}{2}}e^{j(\omega+(2n-1)\omega_m)t}\right.$$
$$\left. - e^{j\frac{(2n-1)\pi}{2}}e^{j(\omega-(2n-1)\omega_m)t}\right). \qquad (13)$$

This gets multiplied with the multiplication factor of the right-hand side mixer, resulting in the output signal shown in the following:

$$v_2^-(t)$$
$$= \left[\frac{2}{j\pi}e^{-j\omega\frac{T_m}{4}}\sum_{n=1}^{\infty}\frac{1}{2n-1}\left(e^{-j\frac{(2n-1)\pi}{2}}e^{j(\omega+(2n-1)\omega_m)t}\right.\right.$$
$$\left.\left. - e^{j\frac{(2n-1)\pi}{2}}e^{j(\omega-(2n-1)\omega_m)t}\right)\right]$$
$$\times \left[\frac{2}{j\pi}\sum_{p=1}^{\infty}\frac{1}{2p-1}\left(e^{-j\frac{(2p-1)\pi}{2}}e^{j(2p-1)\omega_m t}\right.\right.$$
$$\left.\left. - e^{j\frac{(2p-1)\pi}{2}}e^{-j(2p-1)\omega_m t}\right)\right]$$
$$= \frac{-4}{\pi^2}e^{-j\omega\frac{T_m}{4}}\sum_{n=1}^{\infty}\frac{1}{(2n-1)^2}(-e^{j(\omega+(2n-1)\omega_m-(2n-1)\omega_m)t}$$
$$- e^{j(\omega-(2n-1)\omega_m+(2n-1)\omega_m)t})$$
$$= \frac{8}{\pi^2}e^{-j\omega\frac{T_m}{4}}e^{j\omega t}\sum_{n=1}^{\infty}\frac{1}{(2n-1)^2}$$
$$= e^{-j\omega\frac{T_m}{4}}e^{j\omega t}$$
$$= e^{-j\omega\frac{T_m}{4}}v_1^+(t). \qquad (14)$$

This agrees with the result from the time-domain analysis in (8). At frequencies other than the frequency of the input signal, due to cancellation of the intermodulation products, the amplitude of the signal becomes zero, making the structure to appear externally LTI, while being internally LPTV, as mentioned earlier. However, in a practical implementation, the degree of cancellation of the intermodulation products will be limited by the nonidealities, such as dispersion and frequency-dependent quality factor of the transmission lines. For a signal traveling from right to left, the result in (7) can be obtained in the frequency domain as well by following a similar approach.

III. AMPLITUDE NONRECIPROCITY: ISOLATORS AND CIRCULATORS

So far, we have discussed various topologies of spatio-temporal conductivity modulation that realize phase non-reciprocity. In this section, we discuss topologies and circuits exhibiting amplitude nonreciprocity, such as isolators and circulators.

A. Frequency-Conversion Isolator

An isolator is a two-port nonreciprocal component that supports transmission in one direction but not in the reverse direction. A frequency-conversion isolator can be realized from the doubly balanced phase-nonreciprocal element by modifying the delay between the modulation signals of the left-hand side Gilbert-quad switch set $LO_1(t)$ and right-hand side switch set $LO_2(t)$ to a value $T_m/8$, which is also the modified propagation delay of the differential transmission line between the switch sets, as shown in Fig. 4.

A signal traveling from left to right, incident differentially at port 1, transmits to port 2 with no sign inversion in the first half of the modulation cycle and two inversions in the second half of the cycle, similar to the doubly balanced phase-nonreciprocal element. A signal traveling from right to left, incident differentially at port 2, will be transmitted without sign inversion during the first and third quarter cycles. However, during the second and fourth quarter cycles, the signal will be transmitted with a sign inversion from the left and right Gilbert-quad switch sets, respectively, as shown in Fig. 4. Equivalently, the signal traveling from right to left will be multiplied with a $+1/-1$ square wave of 50% duty cycle and $2\omega_m$ angular frequency and gets upconverted/downconverted to other frequencies (i.e., intermodulation products), leading to an isolation at the input frequency. The operation of this structure can be expressed in the time domain as

$$v_1^-(t) = m\left(t - \frac{T_m}{4}\right) \times v_2^+\left(t - \frac{T_m}{8}\right) \times m(t) \quad (15)$$

$$v_2^-(t) = m\left(t - \frac{T_m}{8}\right) \times v_1^+\left(t - \frac{T_m}{8}\right) \times m\left(t - \frac{T_m}{8}\right)$$

$$= v_1^+\left(t - \frac{T_m}{8}\right). \quad (16)$$

The fundamental-to-fundamental S-parameter matrix is obtained by taking Fourier transform of the time-domain
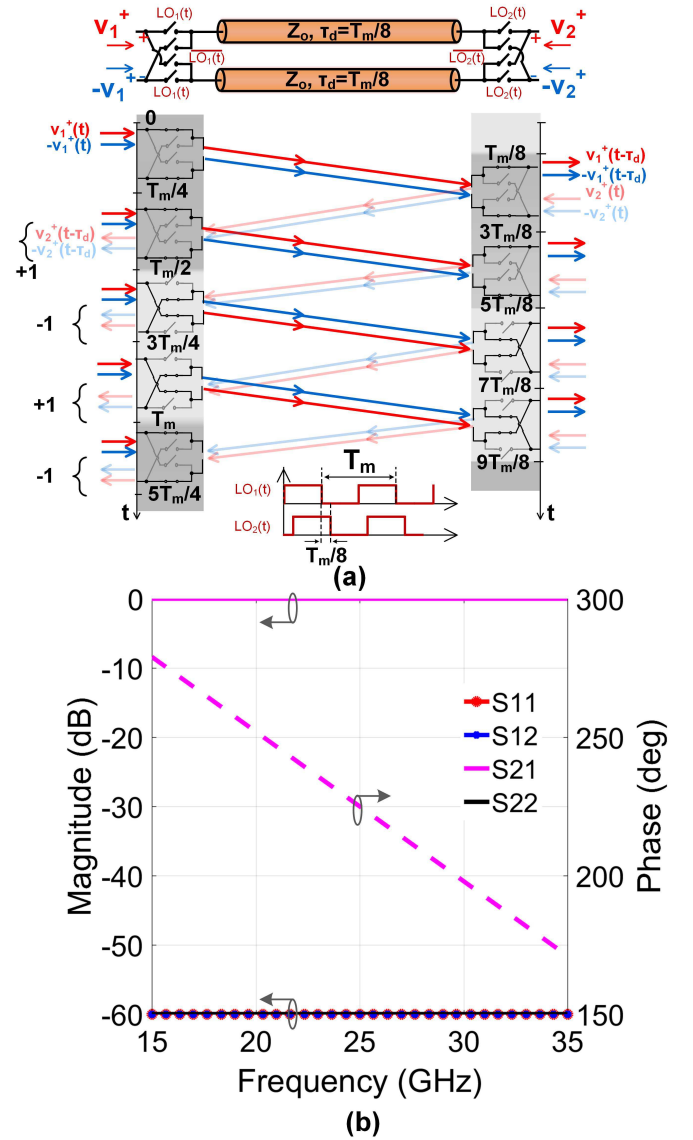

Fig. 4. Frequency-conversion isolator (a) circuit diagram and operation and (b) fundamental-to-fundamental scattering parameters for $f_m = 8.33$ GHz.

equations

$$S = \begin{pmatrix} 0 & 0 \\ +e^{-j\omega\frac{T_m}{8}} & 0 \end{pmatrix}. \quad (17)$$

From (17), it can be seen that the power incident at port 2 at any input frequency gets translated to other frequencies, while the power incident at port 1 is transmitted losslessly, making it a frequency-conversion isolator that can operate over an infinitely wide range of operating frequencies. It should be emphasized, however, that this configuration has limitations when it comes to instantaneously wideband signals at port 2. For signals with bandwidth greater $2\omega_m$, the frequency-translated signals will fall within the desired signal's bandwidth, compromising the isolation from port 2 to port 1. Fig. 4(b) shows the fundamental-to-fundamental S-parameters around 25 GHz for $f_m = 8.33$ GHz.
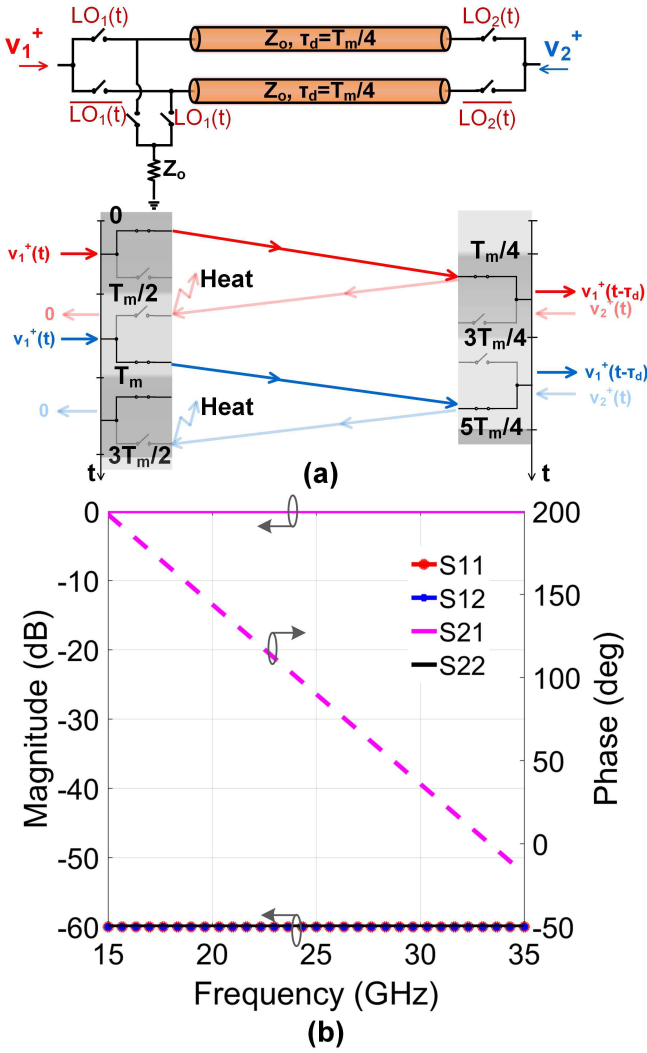
This article has been accepted for inclusion in a future issue of this journal. Content is final as presented, with the exception of pagination.

NAGULU *et al.*: NONRECIPROCAL COMPONENTS BASED ON SWITCHED TRANSMISSION LINES

7

Fig. 5. Ultra-broadband dissipative isolator (a) circuit diagram and operation and (b) scattering parameters for the case with $f_m = 8.33$ GHz.

Fig. 6. Ultra-broadband circulator (a) circuit diagram and (b) scattering parameters for $f_m = 8.33$ GHz.

B. Ultra-broadband Dissipative Isolator

Isolation through frequency conversion is often undesirable, as isolators are typically used to protect sources and amplifiers from back reflections. In such situations, it is desirable for signals incident in the reverse direction to be dissipated within the isolator. Indeed, such perfect isolation and matching cannot be realized without the presence of loss in the system [41]. An ultra-broadband dissipative isolator with no frequency conversion can be realized by modifying the balanced phase-nonreciprocal element by adding a pair of parallel switches with a terminating resistor, of value equal to the port impedance, at the left-hand side switches. The new pair of switches is modulated using the complementary clocks of the left-hand side switches, as shown in Fig. 5. For signals traveling from left to right, this structure behaves exactly like the balanced phase-nonreciprocal element, imparting a delay of $T_m/4$. However, for signals traveling from right to left, after the first pass, instead of reflecting, the signals travel through the newly added switches and get dissipated in the terminating
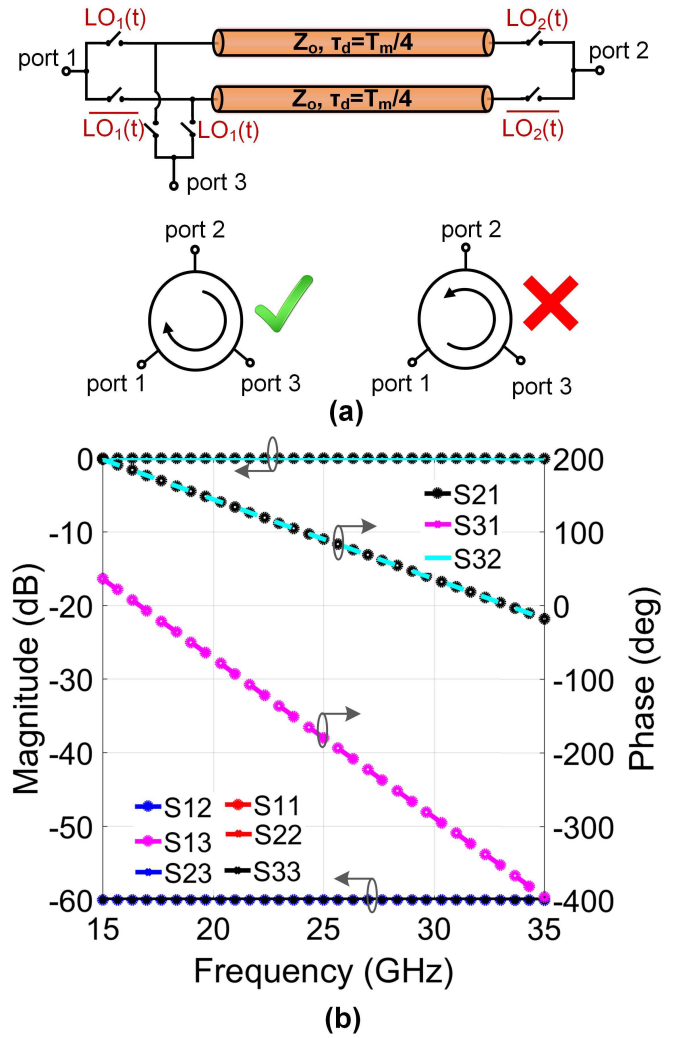
resistor. The operation of the structure can be expressed in the time domain as

$$v_1^-(t) = 0 \tag{18}$$

$$v_2^-(t) = v_1^+\left(t - \frac{T_m}{4}\right). \tag{19}$$

By taking Fourier transform of the time-domain equations, the S-parameter matrix can be calculated as

$$S = \begin{pmatrix} 0 & 0 \\ +e^{-j\omega\frac{T_m}{4}} & 0 \end{pmatrix}. \tag{20}$$

Theoretically, this structure appears externally LTI, exhibits lossless transmission in the forward direction and perfect isolation in the reverse direction, and has infinite bandwidth [see Fig. 5(b)]. In practice, the loss and the bandwidth are limited by the quality factor of transmission line, nonzero switch ON-resistance, dispersion of the transmission line, switch parasitic capacitance, and nonidealities of the modulation clocks, similar to the phase-nonreciprocal elements.

This article has been accepted for inclusion in a future issue of this journal. Content is final as presented, with the exception of pagination.

8

IEEE TRANSACTIONS ON MICROWAVE THEORY AND TECHNIQUES

C. Ultra-Broadband Circulator

The ultra-broadband dissipative isolator is actually a special case of an ultra-broadband circulator whose third port has been terminated to the reference impedance. In other words, a circulator with infinite bandwidth can be realized by replacing the terminating resistor in the ultra-broadband isolator by a third port, as shown in Fig. 6. For such a circulator, it can be shown using the time-domain analysis that lossless transmission happens from port 1 to port 2, port 2 to port 3, and port 3 to port 1, and there will be a perfect isolation in the reverse circulation direction. The S-parameter matrix for this ultra-broadband circulator can be constructed as

$$S = \begin{pmatrix} 0 & 0 & e^{-j\omega\frac{2T_m}{4}} \\ e^{-j\omega\frac{T_m}{4}} & 0 & 0 \\ 0 & e^{-j\omega\frac{T_m}{4}} & 0 \end{pmatrix}. \quad (21)$$

As opposed to three switches in the signal path as in [33], this structure has only two switches, enabling it to potentially have superior insertion loss performance. In addition, this structure needs only two transmission lines as opposed to six transmission lines in [33], making it more compact and readily implementable at RF frequencies. It is closely related to the four-port circulator recently described in [34]. Such an ultra-broadband circulator has a wide range of practical applications, such as STAR: 1) impulse-based communication and radar systems and 2) widely tunable software-defined radio applications.

D. High-Linearity Circulator

The ultra-broadband circulator features switches in the signal path, which would limit the power handling of the circulator, particularly in the TX-to-ANT path. Recently, we demonstrated a circulator architecture with high power handling by wrapping a $3\lambda/4$ transmission line with a characteristic impedance equal to the port impedance around the gyrator component with $\pm 90°$ nonreciprocal phase and placing ports $\lambda/4$ apart on the $3\lambda/4$ transmission line [30]–[32] (see Fig. 7). For such a circulator, the S-parameters at the center frequency can be computed as

$$S = \begin{pmatrix} 0 & 0 & -1 \\ -j & 0 & 0 \\ 0 & -j & 0 \end{pmatrix}. \quad (22)$$

The power handling at port 1 of the circulator (TX port) can be improved significantly by placing the third port at the gyrator element ($l = 0$ in Fig. 7), as the isolation from port 1 to port 3 suppresses the voltage swing across the gyrator [30]. In [30], a 750-MHz circulator was demonstrated in a 65-nm CMOS using the N-path-filter-based gyrator discussed earlier. In [31] and [32], a differential circulator was realized at 25 GHz in the 45-nm SOI CMOS using the doubly balanced transmission-line based gyrator. In general, both single-ended and differential circulators can be realized using the balanced and doubly balanced gyrator configurations [see Fig. 7(a) and (b)]. The balanced configuration achieves gyrator functionality at $\omega = (2n + 1)\omega_m$. The doubly balanced configuration achieves a nonreciprocal phase of π
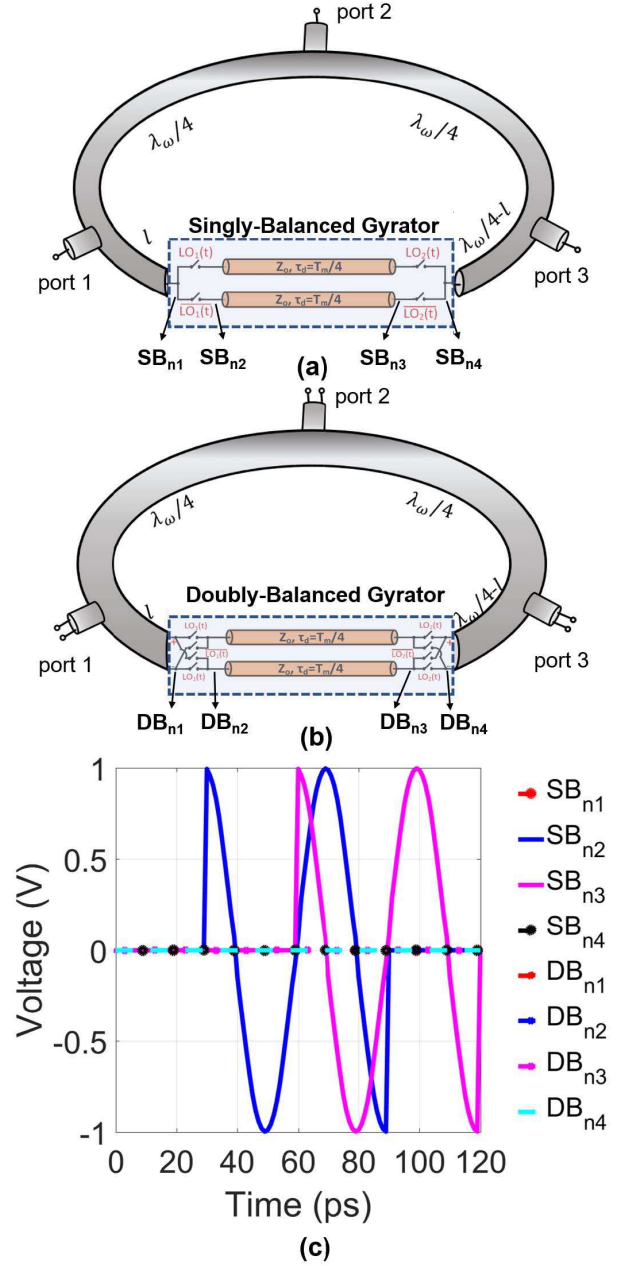

Fig. 7. Highly linear circulators. (a) Single-ended configuration leveraging the balanced gyrator. (b) Differential configuration leveraging the doubly balanced gyrator. (c) Internal node voltage swings of both configurations when $l = 0$ for 1-V TX port voltage at 25 GHz.

across infinite bandwidth, but the need for $\pm 90°$ phase once again dictates $\omega = (2n + 1)\omega_m$. In the 25-GHz circulator in [31] and [32], the modulation frequency was one-third of the operating frequency, which critically enabled scaling of the circulator to millimeter waves. An important point of difference is that the internal gyrator nodes also experience suppressed voltage swing for TX-port excitations in the differential configuration, due to the fact that a pair of switches is always ON, shorting the internal nodes to the external nodes [see Fig. 7(c)]. This, however, is not the case for the single-ended circulator configuration that uses the balanced gyrator, limiting the TX power handling enhancement. This can be

This article has been accepted for inclusion in a future issue of this journal. Content is final as presented, with the exception of pagination.

NAGULU *et al.*: NONRECIPROCAL COMPONENTS BASED ON SWITCHED TRANSMISSION LINES

9

restored by adding a pair of parallel switches to ground at both the left-hand side and right-hand side switches. The new pair of switches would be modulated using the complementary clocks of the original switches, making the nodes SB_{n2} and SB_{n3} quiet. However, due to the additional switches, the power consumption of this single-ended circulator would become equal to that of the differential circulator, and so it is beneficial to implement the differential configuration owing to its benefits of lower clock feedthrough and $+3$-dB higher power handling.

Due to their high linearity, compact reliability, and CMOS integration, these circulators may find application in RF wireless communication systems enabling fully integrable FD solutions [8]–[10]. Integrable millimeter-wave circulators can be used in building relay/repeaters to extend the link range without compromising the channel capacity and can also be utilized in realizing integrated millimeter-wave FMCW radars.

E. Isolation Bandwidth of the High-Linearity Circulator

Isolation from port 1 to port 3 is due to destructive interference of signals from $\lambda/2$ reciprocal path and the $\lambda/4$ transmission line and gyrator path. Perfect isolation occurs at the center frequency where the signals from both paths are exactly out of phase. For frequencies' off center, the condition of destructive interference starts to fail, and isolation will be limited to a finite value. Hence, the isolation bandwidth is dependent on the phase response of the $3\lambda/4$ ring and the non-reciprocal phase response of the gyrator. The doubly balanced gyrator exhibits a nonreciprocal phase response of $180°$ over theoretically infinite bandwidth, while the balanced phase-nonreciprocal element behaves as a gyrator only at discrete frequencies, as discussed earlier.

TX–RX isolation of the high-linearity circulator can be derived as shown in the following:

$$S_{31}(\omega) = S_{21,\lambda/4} \times S_{21,gyr} \times \left(\frac{D \times K_1 - B \times K_2}{AD - BC} \right)$$
$$- \frac{1}{S_{21,\lambda/4} \times S_{12,gyr}} \times \left(\frac{A \times K_2 - C \times K_1}{AD - BC} \right)$$

where

$$A = 6S_{21,\lambda/4} \times S_{12,gyr} - S_{21,\lambda/4}^2$$
$$\times S_{12,gyr} \times S_{21,gyr} \times \left(S_{21,\lambda/4}^2 - 1 \right)$$
$$B = 2S_{21,\lambda/4} \times S_{12,gyr} + S_{21,\lambda/4}^2 + 3$$
$$C = S_{21,\lambda/4}^2 \times S_{12,gyr} \times S_{21,gyr}$$
$$\times \left(S_{21,\lambda/4}^2 + 3 \right) + 2S_{21,\lambda/4}^3 \times S_{12,gyr}$$
$$D = (9 - S_{21,\lambda/4}^2) - 2S_{21,\lambda/4}^3 \times S_{12,gyr}$$
$$K_1 = 4S_{21,\lambda/4} \times S_{12,gyr}, K_2 = 4S_{21,\lambda/4}^3 \times S_{12,gyr} \quad (23)$$

where $S_{21,\lambda/4}$ is the transmission of the $\lambda/4$ transmission line, $S_{21,gyr}$ is the forward transmission, S_{21}, of the gyrator, and $S_{12,gyr}$ is the reverse transmission, S_{12}, of the gyrator. From (6), $S_{21,gyr} = e^{-j(\pi/2)(\omega/\omega_m)}$ and $S_{12,gyr} = e^{-j(3\pi/2)(\omega\omega_m)}$ for the balanced gyrator. From (9), $S_{21,gyr} = e^{-j(\pi/2)(\omega/\omega_m)}$ and $S_{12,gyr} = -e^{-j(\pi/2)(\omega/\omega_m)}$ for the doubly balanced gyrator. As the frequency shifts from the center $((2n+1)\omega_m)$, $S_{12,gyr}$ of the balanced gyrator shifts by a
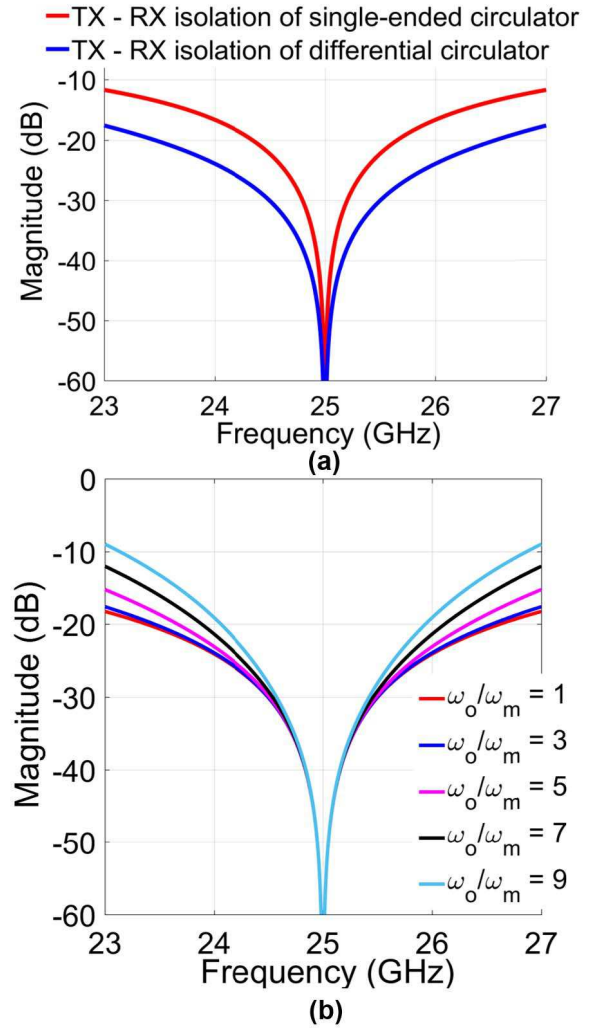

Fig. 8. (a) Port 1–Port 3 isolation of the differential circulator with $\omega_o/\omega_m = 3$ featuring the doubly balanced gyrator and the single-ended circulator with $\omega_o/\omega_m = 3$ featuring the balanced gyrator, shown in Fig. 7(a) and (b). (b) Port 1–Port 3 isolation of the differential circulator featuring the doubly balanced gyrator for various ω_o/ω_m values.

greater value due to the three times factor in the phase. This larger deviation results in a narrower isolation bandwidth when compared with the circulator built using the doubly balanced gyrator. Hence, as shown in Fig. 8(a), the 20-dB isolation bandwidth of the differential circulator featuring the doubly balanced gyrator is 2.34 times higher than that of the single-ended circulator featuring the balanced gyrator.

In addition to the choice of a nonreciprocal element, the choice of modulation frequency also affects the TX–RX isolation bandwidth. At a given offset frequency $(\omega_o + \Delta\omega)$, reducing the modulation frequency results in larger deviation in $S_{21,gyr}$ and $S_{12,gyr}$ from their optimum value for infinite isolation. This larger deviation results in narrower isolation bandwidth. For instance, as shown in Fig. 8(b), the isolation bandwidth of a differential circulator featuring a doubly balanced gyrator decreases when the modulation frequency is decreased. Isolation bandwidth in the presence of finite quality factor of the transmission lines can be
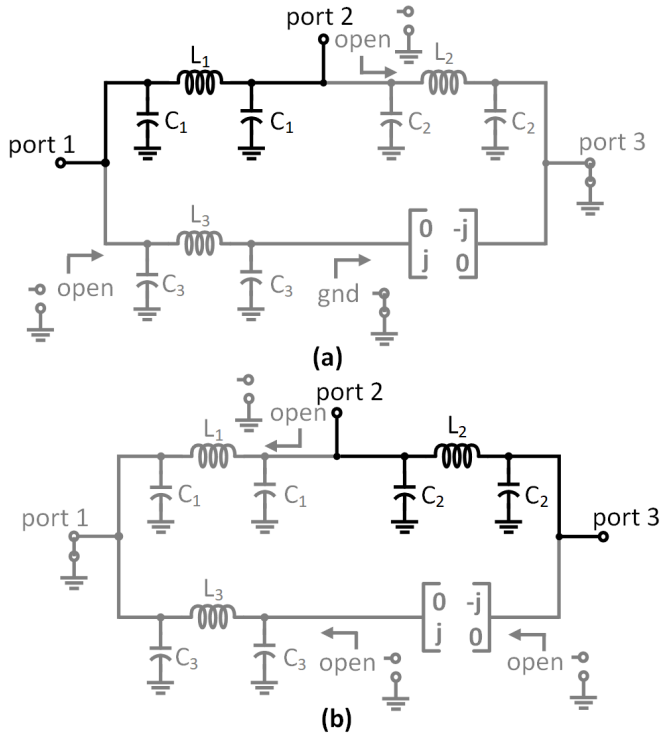
This article has been accepted for inclusion in a future issue of this journal. Content is final as presented, with the exception of pagination.

10

IEEE TRANSACTIONS ON MICROWAVE THEORY AND TECHNIQUES

Fig. 9. (a) Equivalent circuit for loss estimation from port 1 to port 2. (b) Equivalent circuit for loss estimation from port 2 to port 3.
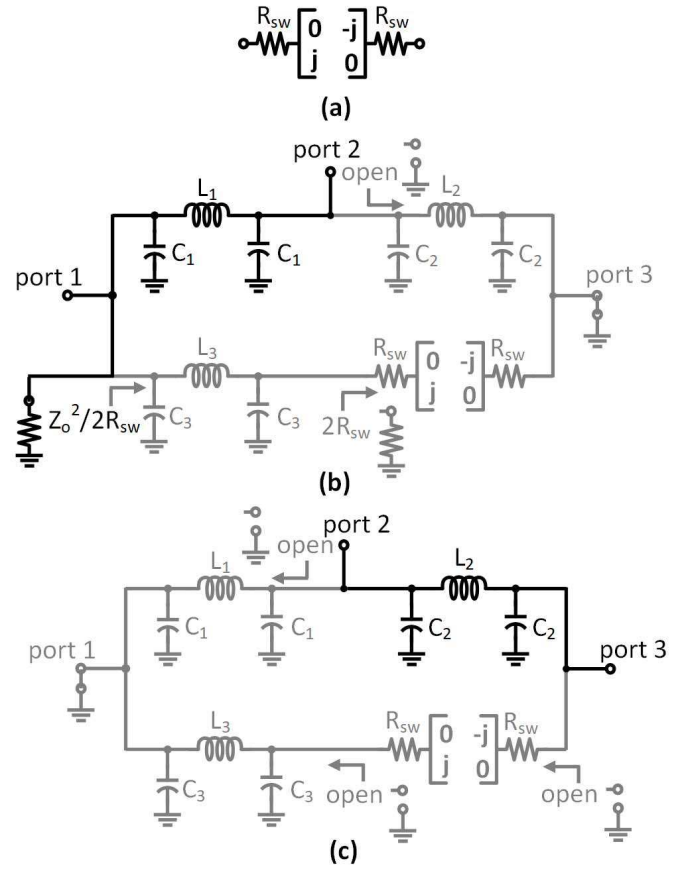

Fig. 10. (a) Equivalent circuit for a gyrator with nonzero switch resistance. (b) Equivalent circuit for loss estimation from port 1 to port 2 of the circulator with nonzero switch resistance. (c) Equivalent circuit for loss estimation from port 2 to port 3 of the circulator with nonzero switch resistance.

easily calculated by modifying $S_{21,\lambda/4}$, $S_{21,gyr}$, and $S_{12,gyr}$. For a single-ended circulator built using transmission lines of quality factor Q, $S_{21,\lambda/4} = e^{-((1/2Q)+j)(\pi/2)(\omega/\omega_o)}$, $S_{21,gyr} = e^{-((1/2Q)+j)(\pi/2)(\omega/\omega_m)}$, and $S_{12,gyr} = e^{-((1/2Q)+j)(3\pi/2)(\omega/\omega_m)}$. Similarly, for a differential circulator built using transmission lines of quality factor Q, $S_{21,\lambda/4} = e^{-((1/2Q)+j)(\pi/2)(\omega/\omega_o)}$, $S_{21,gyr} = e^{-((1/2Q)+j)(\pi/2)(\omega/\omega_m)}$, and $S_{12,gyr} = -e^{-((1/2Q)+j)(\pi/2)(\omega/\omega_m)}$.

IV. ANALYSIS OF INSERTION LOSS BASED ON VARIOUS NONIDEALITIES

In this section, we derive formulas for estimating the transmission losses of the highly linear circulator architecture taking various nonidealities into account using perturbation analysis. During implementation, transmission lines of length comparable to the wavelength are often miniaturized using lumped L–C components to reduce the chip area and to absorb the parasitic capacitances of the switches into the transmission lines. Hence, in our analysis, it is assumed that the $\lambda/4$ transmission lines sections in the $3\lambda/4$ ring were miniaturized using C–L–C sections. Various nonidealities, such as quality factor of the transmission lines/inductors, nonzero switch resistance of the switches in the gyrator element, rise/fall time of the modulation signals, and the dispersion of the transmission line in the gyrator, limit the insertion loss of the circulator. In this derivation, it has been assumed that the effect of the nonidealities is small, so that they do not degrade the matching of the gyrator element and the isolation of the circulator substantially. The effect of each nonideality in the circulator is separately computed using perturbation analysis, and the

total loss of the circulator is estimated by summing up the individual contributions.

While estimating the loss from port 1 to port 2 in the circulator, port 3 can be shorted to ground due to the port 1-to-port 3 isolation. As a result, the $\lambda/4$ section between port 2 and port 3 will transform the short circuit to an open circuit when seen from port 2 as will the $\lambda/4$ section between port 1 and the gyrator when seen from port 1. Hence, the circulator reduces to a $\lambda/4$ transmission line connecting ports 1 and 2, as shown in Fig. 9(a). A similar equivalent circuit for port 2-to-port 3 transmission is shown in Fig. 9(b).

A. Effect of Nonzero Switch Resistance R_{sw}

A switch with nonzero ON-resistance R_{sw} can be modeled by an ideal switch with a series resistance R_{sw}. Hence, a gyrator with nonzero switch resistance can be modeled in the manner shown in Fig. 10(a). As before, port 3 of the circulator can be shorted to ground when estimating the loss from port 1 to port 2, as shown in Fig. 10(b). When one of its ports is shorted to ground, the input impedance of the gyrator shown in Fig. 10(a) at the other port is $2R_{sw}$. This $2R_{sw}$ resistance will be transformed to $Z_0^2/2R_{sw}$ at port 1, as shown in Fig. 10(b). Consequently, the transmission loss
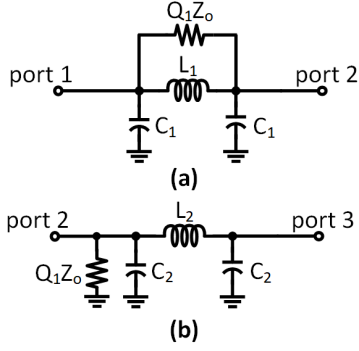
This article has been accepted for inclusion in a future issue of this journal. Content is final as presented, with the exception of pagination.

NAGULU *et al.*: NONRECIPROCAL COMPONENTS BASED ON SWITCHED TRANSMISSION LINES

11

Fig. 11. Equivalent circuits for loss estimation of the circulator with finite quality factor Q_1 in inductor L_1. (a) Port 1 to port 2. (b) Port 2 to port 3.

from port 1 to port 2 can be written as

$$|S_{21}| \approx \frac{Z_0}{Z_0 + R_{sw}} = \frac{Q_{sw}}{Q_{sw} + 1} \tag{24}$$

where Q_{sw}, the *equivalent* quality factor of the switch, is given by Z_0/R_{sw}. Similarly, port 1 can be shorted to ground while estimating transmission loss from port 2 to port 3. Using similar arguments, the circulator can be reduced to the circuit shown in Fig. 10(c). Interestingly, the nonzero switch resistance will have no effect on the transmission loss from port 2 to port 3 because the switch resistance is in series with an open termination

$$|S_{32}| \approx 1. \tag{25}$$

B. Effect of the Quality Factor Q_1 of Inductor L_1

Similar arguments can be made for the quality factor Q_1 of inductor L_1. Fig. 11(a) and (b) shows the equivalent circuits for S_{21} and S_{32} loss estimation. We have assumed that the inductor losses are purely in the form of series resistance in writing the equivalent parallel resistance as $\omega L_1 Q_1 = Q_1 Z_0$. Furthermore, we have assumed that the capacitors used to lump the transmission line are lossless. By analyzing these circuits, we can write the transmission losses as

$$|S_{21}| \approx \left| \frac{\left(\frac{1}{Q_1} - j\right)}{\left(1 + \frac{1}{Q_1}\right) + \frac{j}{Q_1}} \right| \approx \frac{Q_1}{Q_1 + 1} \tag{26}$$

$$|S_{32}| \approx \frac{2Q_1}{2Q_1 + 1}. \tag{27}$$

C. Effect of the Quality Factor Q_2 of Inductor L_2

Making similar arguments, the equivalent circuits in Fig. 12 enable loss estimation in the presence of finite quality factor Q_2 in inductor L_2. By analyzing these circuits, we can write the transmission losses as

$$|S_{21}| \approx \frac{2Q_2}{2Q_2 + 1} \tag{28}$$

$$|S_{32}| \approx \left| \frac{\left(\frac{1}{Q_2} - j\right)}{\left(1 + \frac{1}{Q_2}\right) + \frac{j}{Q_2}} \right| \approx \frac{Q_2}{Q_2 + 1}. \tag{29}$$
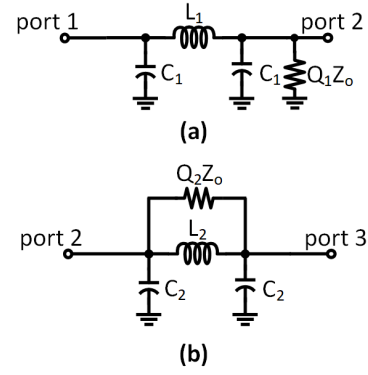

Fig. 12. (a) Equivalent circuit for loss estimation from port 1 to port 2 of the circulator with inductor L_2 of finite quality factor Q_2. (b) Equivalent circuit for loss estimation from port 2 to port 3 of the circulator with inductor L_2 of finite quality factor Q_2.
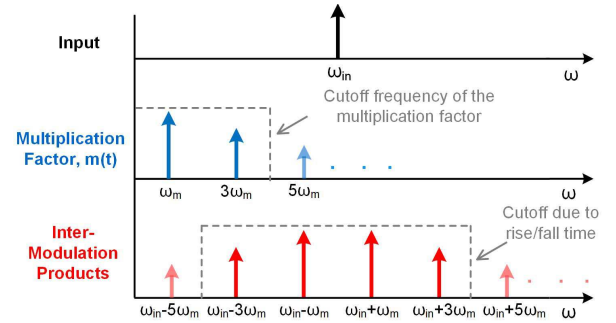

Fig. 13. Filtering due to finite rise/fall time of the modulation signals.

D. Effect of the Quality Factor Q_3 of Inductor L_3

Similarly, the circulator with finite quality factor Q_3 in inductor L_3 can be reduced to a $C–L–C$ section with a shunt resistor $Q_3 Z_0$ at port 1 while estimating loss from port 1 to port 2 and a $C–L–C$ section with a shunt resistor $Q_3 Z_0$ at port 3 while estimating loss from port 2 to port 3. By analyzing these circuits, we can write the transmission losses as

$$|S_{21}| \approx \frac{2Q_3}{2Q_3 + 1} \tag{30}$$

$$|S_{32}| \approx \frac{2Q_3}{2Q_3 + 1}. \tag{31}$$

E. Effect of the Rise/Fall Time of the Modulation Signal

In Section II-D, we have presented a frequency domain of the doubly balanced ultra-broadband gyrator with the switch sets viewed as mixers. We considered the modulation signals to be perfect square waves with negligible rise/fall time, but in a practical implementation, the rise/fall time (t_r/t_f) can be a significant portion of the time period, particularly for high-frequency operation. For a trapezoidal modulation signal with rise/fall time of $t_r = t_f$, the frequency content of the modulation signal will be limited to a cutoff frequency of $(0.35/t_r)$ Hz. This will correspondingly establish an upper limit on the frequency content of the multiplication factor $m(t)$ as shown in Fig. 13. The value of this cutoff frequency can be obtained from simulations. The effect of this cutoff frequency

This article has been accepted for inclusion in a future issue of this journal. Content is final as presented, with the exception of pagination.

12

IEEE TRANSACTIONS ON MICROWAVE THEORY AND TECHNIQUES

in the multiplication factor is a limit to the intermodulation products that are generated and travel down the line, as shown in Fig. 13, resulting in the loss of signal power. In our analysis, the filtering profile of this effect is assumed to be a brick wall, and mathematically, this can be expressed as a truncation in the higher frequency terms in (10)–(14). For the example shown in Fig. 13, where the cutoff frequency is between $3\omega_m$ and $5\omega_m$, (14) can be modified as

$$
\begin{aligned}
v_2^-(t) \\
&= \frac{-4}{\pi^2} e^{-j\omega\frac{T_m}{4}} \left[(-e^{j(\omega+\omega_m-\omega_m)t} - e^{j(\omega-\omega_m+\omega_m)t}) \right. \\
&\qquad \left. + \frac{1}{3^2} (-e^{j(\omega+3\omega_m-3\omega_m)t} - e^{j(\omega-3\omega_m+3\omega_m)t}) \right] \\
&= \frac{80}{9\pi^2} e^{-j\omega\frac{T_m}{4}} e^{j\omega t} \\
&= \frac{80}{9\pi^2} e^{-j\omega\frac{T_m}{4}} v_1^+(t) \\
&\approx 0.9 e^{-j\omega\frac{T_m}{4}} v_1^+(t).
\end{aligned}
\tag{32}
$$

Similarly, for the signal traveling from right to left, the signal transmitted can be written as

$$
v_1^-(t) \approx -0.9 e^{-j\omega\frac{T_m}{4}} v_1^+(t).
\tag{33}
$$

Assuming that the matching of the gyrator has not degraded due to the finite rise and fall time, the S-parameter matrix of the gyrator at the center frequency can be written as

$$
S = \begin{pmatrix} 0 & k_{\text{rise/fall}} e^{j\frac{\pi}{2}} \\ k_{\text{rise/fall}} e^{-j\frac{\pi}{2}} & 0 \end{pmatrix}
\tag{34}
$$

where $k_{\text{rise/fall}}$ is the attenuation factor due to the filtering of higher intermodulation products. For the example shown in Fig. 13, $k_{\text{rise/fall}} \approx 0.9$. Using the perturbation analysis discussed before, the S-parameters of the circulator can be expressed as

$$
|S_{21}| \approx \frac{Q_{\text{rise/fall}}}{Q_{\text{rise/fall}} + 1}
\tag{35}
$$

$$
|S_{32}| \approx \frac{Q_{\text{rise/fall}}}{Q_{\text{rise/fall}} + 1}
\tag{36}
$$

where $Q_{\text{rise/fall}}$ is an *effective* quality factor associated with the filtering due to finite rise/fall time of the modulation signals and is given by $2(1 + k_{\text{rise/fall}}^2)/(1 - k_{\text{rise/fall}}^2)$.

F. Effect of the Bragg Frequency of the Gyrator Transmission Line

From the frequency-domain analysis, it is clear that the transmission line(s) between the switches must be able to support all the intermodulation frequencies with the same group delay for a perfect lossless gyrator. If the transmission lines are miniaturized through a quasi-distributed implementation consisting of periodic lumped-LC sections, then the lines will have a cutoff frequency, after which the periodic structure no longer supports a traveling wave. This cutoff frequency is known as the Bragg frequency. Intermodulation products above the Bragg frequency will be filtered, and the signal power associated with them will be lost as shown
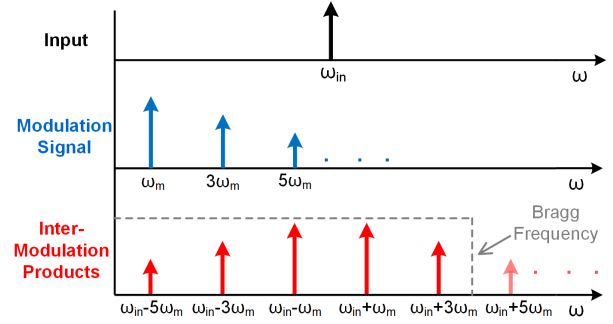

Fig. 14. Filtering of the intermodulation products higher than the Bragg Frequency.

in Fig. 14. Similar to the effect of finite rise and fall time of the modulation signal, the filtering profile due to Bragg frequency is also assumed to be a brick wall. All the intermodulation terms with frequency above the Bragg frequency should be truncated from (14), and an associated attenuation factor k_{Bragg} can be calculated. Assuming that the matching of the gyrator has not degraded due to Bragg frequency effects, the S-parameter matrix of the gyrator at the center frequency can be written as

$$
S = \begin{pmatrix} 0 & k_{\text{Bragg}} e^{j\frac{\pi}{2}} \\ k_{\text{Bragg}} e^{-j\frac{\pi}{2}} & 0 \end{pmatrix}.
\tag{37}
$$

From a similar perturbation analysis, the S-parameters of the circulator can be expressed as

$$
|S_{21}| \approx \frac{Q_{\text{Bragg}}}{Q_{\text{Bragg}} + 1}
\tag{38}
$$

$$
|S_{32}| \approx \frac{Q_{\text{Bragg}}}{Q_{\text{Bragg}} + 1}
\tag{39}
$$

where Q_{Bragg} is an effective quality factor associated with the Bragg effect and is given by $2(1 + k_{\text{Bragg}}^2)/(1 - k_{\text{Bragg}}^2)$.

Both finite rise/fall time and finite Bragg frequency result in suppressing the higher frequency content of the intermodulation products. Hence, one has to be careful while truncating the terms in (14) because the minimum of these cutoff frequencies will define the actual cutoff frequency for the intermodulation products. In the final loss estimation, to avoid the repetition of the loss due to filtering of higher modulation products, a general attenuation factor k_{filter} can be calculated by truncating all the terms that are required to be truncated from Bragg frequency effects and finite rise/fall time effects. In general, for circulators operating at high frequencies, finite rise/fall time effects will dominate, while for circulators operating at lower frequencies, the need to aggressively miniaturize the transmission lines will cause Bragg frequency effects to dominate. For instance, in the 25-GHz 45-nm SOI CMOS circulator case study presented later in this paper, truncation was limited by the rise/fall time of the modulation signal, making $k_{\text{filter}} = k_{\text{rise/fall}}$.

G. Effect of the Quality Factor Q_{NR} of the Gyrator Transmission Line

Due to ohmic losses, the signal attenuates exponentially as it travels through the transmission line in the gyrator, creating

This article has been accepted for inclusion in a future issue of this journal. Content is final as presented, with the exception of pagination.

NAGULU *et al.*: NONRECIPROCAL COMPONENTS BASED ON SWITCHED TRANSMISSION LINES 13

another loss mechanism. As mentioned earlier, all intermodulation products travel through the transmission line, and the attenuation suffered by each intermodulation product is different because the attenuation constant depends on frequency. The attenuation suffered by a signal at a frequency ω as it travels through the transmission line with a delay of $T_m/4$ is $e^{-(\pi/4Q)(\omega/\omega_m)}$, where Q is the quality factor of the transmission line at ω. Due to the skin effect, $\rho \propto \sqrt{\omega}$, where ρ is the resistivity of the metal. A general attenuation factor can be written by taking the skin effect of the metal into consideration as $e^{-((2n+1)\pi)/(4Q_{NR})(\omega/((2n+1)\omega_m))^{1/2}}$, where Q_{NR} is the quality factor of the transmission line at a frequency $\omega = (2n+1)\omega_m$. By modifying (13), the signal after traveling through the transmission line can be expressed as shown in the following:

$$
v_1^+ \left(t - \frac{T_m}{4}\right) \times m\left(t - \frac{T_m}{4}\right)
$$

$$
= \frac{2}{j\pi} e^{-j\omega \frac{T_m}{4}} \sum_{p=1}^{\infty} \frac{1}{2p-1}
$$

$$
\times \left(e^{-j\frac{(2p-1)\pi}{2}} e^{-\frac{(2n+1)\pi}{4Q_{NR}} \sqrt{\frac{\omega+(2p-1)\omega_m}{(2n+1)\omega_m}}} e^{j(\omega+(2p-1)\omega_m)t} \right.
$$

$$
\left. - e^{j\frac{(2p-1)\pi}{2}} e^{-\frac{(2n+1)\pi}{4Q_{NR}} \sqrt{\frac{|\omega-(2p-1)\omega_m|}{(2n+1)\omega_m}}} e^{j(\omega-(2p-1)\omega_m)t} \right). \quad (40)
$$

This signal gets multiplied with the multiplication factor of the right-hand side mixer. Similar to (14), the signal voltage at the input frequency ω at the other port of the gyrator can be written as shown in the following:

$$
v_2^-(t) = e^{-j\omega \frac{T_m}{4}} e^{j\omega t} \times \frac{4}{\pi^2} \sum_{p=1}^{\infty} \frac{1}{(2p-1)^2}
$$

$$
\times \left(e^{-\frac{(2n+1)\pi}{4Q_{NR}} \sqrt{\frac{\omega+(2p-1)\omega_m}{(2n+1)\omega_m}}} + e^{-\frac{(2n+1)\pi}{4Q_{NR}} \sqrt{\frac{|\omega-(2p-1)\omega_m|}{(2n+1)\omega_m}}} \right)
$$

$$
= e^{-j\omega \frac{T_m}{4}} e^{j\omega t} k_{Q_{NR21}}
$$

$$
= e^{-j\omega \frac{T_m}{4}} v_1^+(t) k_{Q_{NR21}} \quad (41)
$$

where $k_{Q_{NR21}}$ is the attenuation factor for signals traveling from left to right due to the finite quality factor of the transmission line in the gyrator. For a more accurate expression that includes the effects due to the finite Bragg frequency of the line and finite rise and fall times in the modulation signals, the higher intermodulation terms in (41) should be truncated, and the obtained $(k_{Q_{NR21}})_{truncated}$ value should be divided by k_{filter}, i.e., $k_{Q_{NR21}} = (k_{Q_{NR21}})_{truncated}/k_{filter}$, so that $k_{Q_{NR21}}$ isolates the effect of the transmission lines' finite quality factor. Similarly, $k_{Q_{NR12}}$ can be calculated for signals traveling from right to left.

For the balanced gyrator, $k_{Q_{NR12}}$ and $k_{Q_{NR21}}$ will be different because the signals follow a different path for forward and reverse directions, and the attenuation factor depends on the length traversed. However, for the doubly balanced gyrator, these factors will be equal, since the phase nonreciprocity is achieved due to sign inversion from the quad-mixer, rather than path length differences. Assuming that the matching of the gyrator has not degraded due to the quality factor of the transmission line, the S-parameter matrix of the gyrator at the center frequency can be written as

$$
S = \begin{pmatrix} 0 & k_{Q_{NR12}} e^{j\frac{\pi}{2}} \\ k_{Q_{NR21}} e^{-j\frac{\pi}{2}} & 0 \end{pmatrix}. \quad (42)
$$

From the perturbation analysis, the S-parameters of the circulator can be expressed as

$$
|S_{21}| \approx \frac{Q_{NR_{effec}}}{Q_{NR_{effec}} + 1} \quad (43)
$$

$$
|S_{32}| \approx \frac{Q_{NR_{effec}}}{Q_{NR_{effec}} + 1} \quad (44)
$$

where $Q_{NR_{effec}}$ is the effective quality factor associated with the loss of the transmission line in the gyrator and is given by $2((1 + k_{Q_{NR12}} k_{Q_{NR21}})/(1 - k_{Q_{NR12}} k_{Q_{NR21}}))$.

H. Estimating Transmission Losses of the Circulator

Under the assumption that all the nonidealities are small, the losses due to the individual effects can be added when estimating the final loss of the circulator. Hence, the transmission S-parameters of the circulator can be expressed as

$$
|S_{21}| \approx \left(\frac{Q_1}{Q_1 + 1}\right) \left(\frac{2Q_2}{2Q_2 + 1}\right) \left(\frac{2Q_3}{2Q_3 + 1}\right) \left(\frac{Q_{filter}}{Q_{filter} + 1}\right)
$$

$$
\times \left(\frac{Q_{NR_{effec}}}{Q_{NR_{effec}} + 1}\right) \left(\frac{Q_{sw}}{Q_{sw} + 1}\right) \quad (45)
$$

$$
|S_{32}| \approx \left(\frac{2Q_1}{2Q_1 + 1}\right) \left(\frac{Q_2}{Q_2 + 1}\right) \left(\frac{2Q_3}{2Q_3 + 1}\right)
$$

$$
\times \left(\frac{Q_{filter}}{Q_{filter} + 1}\right) \left(\frac{Q_{NR_{effec}}}{Q_{NR_{effec}} + 1}\right). \quad (46)
$$

I. Effect of Timing Errors in the Modulation Clocks

In addition to parasitic losses, timing errors in the modulation clocks can also result in an additional insertion loss, especially when operating at millimeter-wave frequencies. One such timing error is when the delay of the transmission line in the gyrator or the delay between the left-hand side and right-hand side modulation signals deviates from $T_m/4$. Duty-cycle impairment in the modulation clock is another imperfection which can result in additional insertion loss. Interested readers are directed to [42] for a detailed analysis on the effect of timing errors.

V. DISCRETE-COMPONENT-BASED CASE STUDIES

A. Balanced Arbitrary-Phase Nonreciprocal Element

A balanced arbitrary-phase nonreciprocal element has been implemented using coaxial cables and commercially available off-the-shelf switches as shown in Fig. 15. It consists of two 10 m long, 50-Ω coaxial cables with a time delay of 40.5 ns and an insertion loss of 1 dB. These cables are sandwiched between two single-pole double-throw switches, which are modulated at 6.17 MHz. In practice, open-reflective switches with fast switching time are not commercially available. Alternatively, we used short-reflective switches from minicircuits (model number ZFSW-2-46) with a fast switching time of 2 ns, to minimize the insertion loss due to rise/fall time

This article has been accepted for inclusion in a future issue of this journal. Content is final as presented, with the exception of pagination.

14
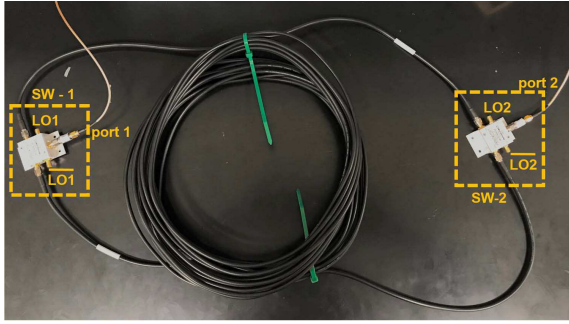
IEEE TRANSACTIONS ON MICROWAVE THEORY AND TECHNIQUES

Fig. 15. Photograph of the balanced arbitrary-phase nonreciprocal element assembly.

as discussed in Section IV. Using a short-reflective switch does not change the principle of operation of the structure. Signals traveling in the forward direction do not see the short termination. However, signals traveling in the reverse direction experience two reflections from a short termination ($\Gamma = -1$) instead of two reflections from an open termination ($\Gamma = 1$). The two additional negative signs cancel each other and result in an output signal that is equal to the open-reflective switch case. At 10 MHz, the switch has an insertion loss of 0.5 dB in the ON state and a reflection coefficient of $0.71\angle 178°$ in the OFF state. The modulation signals are generated using the arbitrary waveform generators (model: Agilent 33500B) and have a rise/fall time of 8.5 ns.

The measured S-parameters between 0 and 50 MHz are shown in Fig. 16. A nonreciprocal phase of 180° has been observed at 6.043, 18.11, and 30.2 MHz. This shift in the gyration frequency is due to the reflection coefficient of the OFF-state switch, which is 178° instead of 180°. Since the reverse traveling wave is reflected twice, a total of $-4°$ phase shift is picked up by the signal. Due to this additional phase shift, the structure behaves as a gyrator at slightly lower frequencies, a similar effect to the observation in [35]. At 10 MHz, the transmission losses in the forward and reverse directions are 3.8 and 17 dB, respectively. The transmission losses in the reverse direction are higher due to the additional loss mechanisms, including three times loss of the transmission line due to reflections, nonunity reflection coefficient of the reflective-short switch in its OFF state ($S_{11} = -3$ dB instead of 0 dB), and destructive interference between the leaked signal to port 1 during OFF state (due to imperfect clocking which is limited by the time resolution of the arbitrary waveform generator) and the actual signal. The accuracy of synchronization between the modulation signals is limited by the arbitrary waveform generator used and has a time resolution of 4 ns.

Based on the loss mechanisms discussed earlier, the signal traveling in the forward direction experiences a transmission loss of 1 dB due to the cable loss, 1 dB from the switches, and 0.7 dB due to the finite rise/fall time and some additional loss due to timing errors. In practice, finite time resolution of the modulation signals can produce overlap between complementary clocks, which affect the duty cycle and delay between the clocks. For simplicity, let us consider the only timing
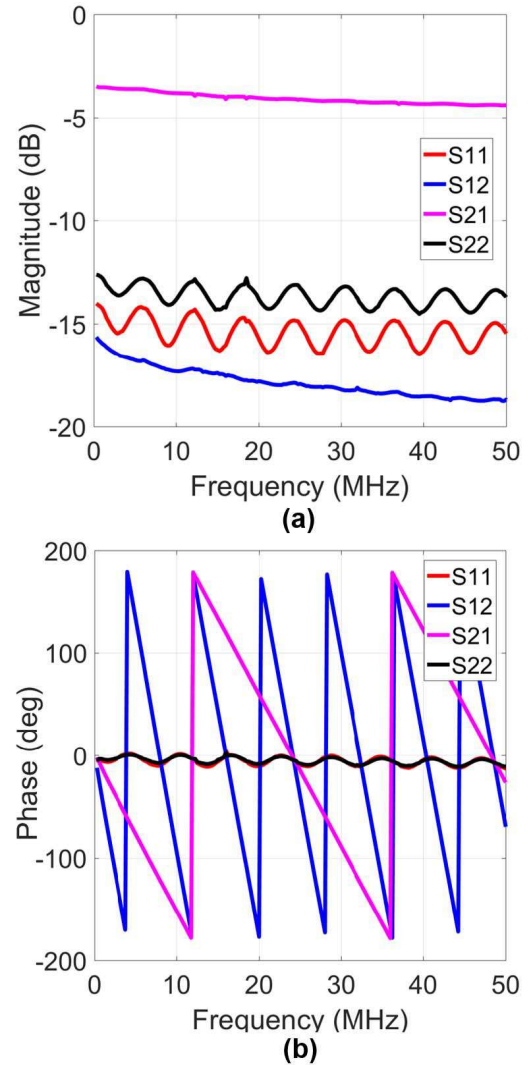

Fig. 16. Measured S-parameters of the balanced arbitrary-phase nonreciprocal element. (a) Magnitude. (b) Phase.

error present to be the delay between $LO_1(t)$ and $LO_2(t)$ with an error Δ_e of 4 ns. From [42, eq. (5)], this results in an additional transmission loss of 0.9 dB. On whole, the estimated transmission loss in the forward direction is $\approx$3.6 dB. Similarly, the transmission in the reverse direction can be calculated. From our estimation, the signal incident at port 2 gets transmitted to port 1 after one pass and three passes with transmission losses of 22.7 and 11.6 dB, respectively. These signals add destructively, resulting in the estimated reverse transmission loss of -14.4 dB.

B. Ultra-Broadband Dissipative Isolator

An ultra-broadband dissipative isolator has been implemented by replacing the left-side switch (SW-1) in the balanced configuration setup with a commercially available absorptive switch from minicircuits (model number: ZFSWA-2-46). The measured S-parameters between 0 and 50 MHz are shown in Fig. 17. The transmission loss in the forward direction ranges from 3.2 to 5.6 dB
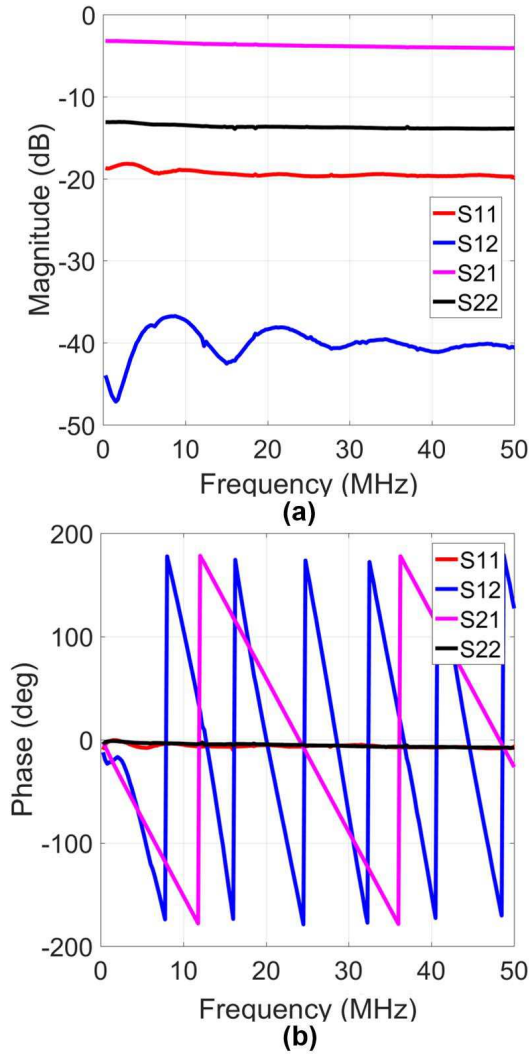
Fig. 17. Measured S-parameters of the ultra-broadband dissipative isolator. (a) Magnitude. (b) Phase.

over the frequency range from dc to 50 MHz. At 10 MHz, the transmission loss of 3.5 dB has been measured. The isolation in the reverse direction is $\approx$40 dB over the entire frequency range.

VI. 25-GHz 45-nm SOI CMOS CIRCULATOR CASE STUDY

A. Implementation Details

A differential circulator based on the doubly balanced gyrator was implemented at 25 GHz in the 45-nm SOI CMOS, as shown in Fig. 18. Aside from achieving superior isolation bandwidth due to the use of the doubly balanced gyrator, the fully differential architecture reduces LO feedthrough and enables 3-dB higher power handling at the expense of a doubling in the power consumption. The quarter-wave sections between ports 1 and 2 and 2 and 3 were implemented using differential conductor-backed coplanar waveguides with Q of 15 at 25 GHz. The gyrator element was placed symmetrically between port 1 and port 3 so that the parasitic capacitances from the mixer switches could be absorbed into
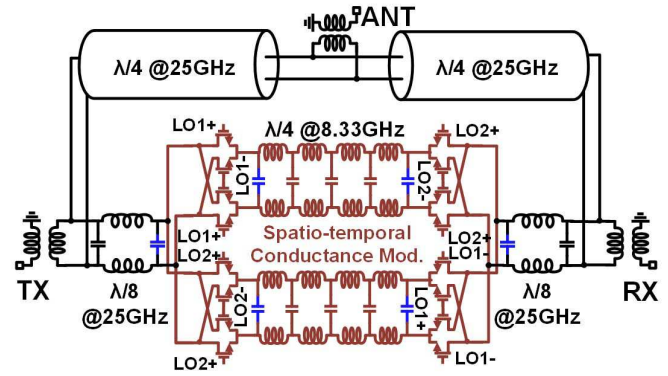

Fig. 18. Circuit diagram of the implemented 25-GHz doubly balanced circulator.

the quasi-distributed transmission line in the gyrator and the $\lambda/8$ C–L–C sections on either side. The transmission line in the gyrator is a combination of four π-type C–L–C sections, with inductor Q of 20, and coplanar waveguides, with Q of 15, connecting the C–L–C sections. The overall quality factor and Bragg frequency of the transmission line are 17 and 83.9 GHz, respectively. The Bragg frequency was improved by a factor of two because only a part of the quarter-period delay required was obtained from the four C–L–C sections, with the rest obtained from the coplanar waveguides used for interconnects. An extra quadrature phase path was added in the gyrator element to counter the loss degradation due to duty-cycle impairments. The reader is directed to [42] for additional details. The Gilbert quad-mixers are designed using 2×16 μm/40 nm floating body transistors, achieving R_{sw} of 8.66 Ω. The placement of the gyrator symmetrically between port 1 and port 3 distributes the loss due to nonzero switch ON-resistance equally between S_{21} and S_{32}, as opposed to (24) and (25). The new transmission losses due to nonzero ON-resistance can be expressed as

$$|S_{21}| \approx \frac{2Q_{\text{sw}}}{2Q_{\text{sw}} + 1} \tag{47}$$

$$|S_{32}| \approx \frac{2Q_{\text{sw}}}{2Q_{\text{sw}} + 1} \tag{48}$$

modifying the circulator transmission losses in (45) and (46) to

$$|S_{21}| \approx \left(\frac{Q_1}{Q_1 + 1}\right)\left(\frac{2Q_2}{2Q_2 + 1}\right)\left(\frac{2Q_3}{2Q_3 + 1}\right)\left(\frac{Q_{\text{filter}}}{Q_{\text{filter}} + 1}\right)$$
$$\times \left(\frac{Q_{\text{NR}_{\text{effec}}}}{Q_{\text{NR}_{\text{effec}}} + 1}\right)\left(\frac{2Q_{\text{sw}}}{2Q_{\text{sw}} + 1}\right) \tag{49}$$

$$|S_{32}| \approx \left(\frac{2Q_1}{2Q_1 + 1}\right)\left(\frac{Q_2}{Q_2 + 1}\right)\left(\frac{2Q_3}{2Q_3 + 1}\right)\left(\frac{Q_{\text{filter}}}{Q_{\text{filter}} + 1}\right)$$
$$\times \left(\frac{Q_{\text{NR}_{\text{effec}}}}{Q_{\text{NR}_{\text{effec}}} + 1}\right)\left(\frac{2Q_{\text{sw}}}{2Q_{\text{sw}} + 1}\right). \tag{50}$$

Fig. 19 shows the circuit diagram of the 8.33-GHz clock path. A two-stage poly-phase filter is used to generate the 8.33-GHz quadrature signals driving the mixer switches. After the poly-phase filter, a three-stage self-biased CMOS buffer chain with inductive peaking in the final stage generates the square-wave clock signals with a rise/fall time of 7.5 ps for
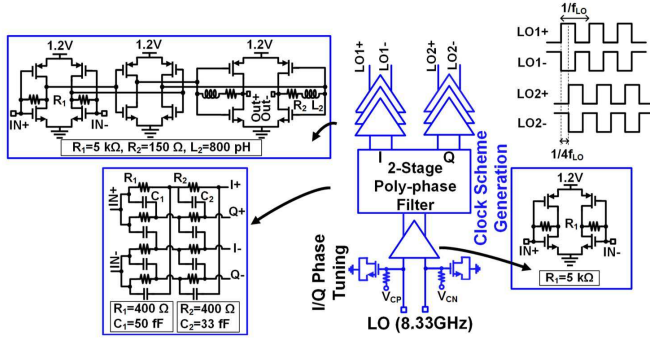
This article has been accepted for inclusion in a future issue of this journal. Content is final as presented, with the exception of pagination.

16

IEEE TRANSACTIONS ON MICROWAVE THEORY AND TECHNIQUES

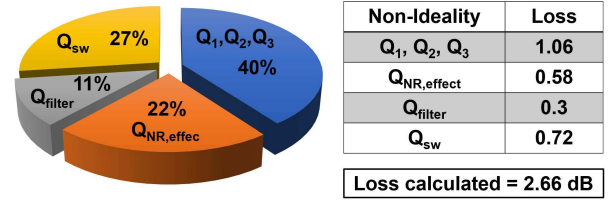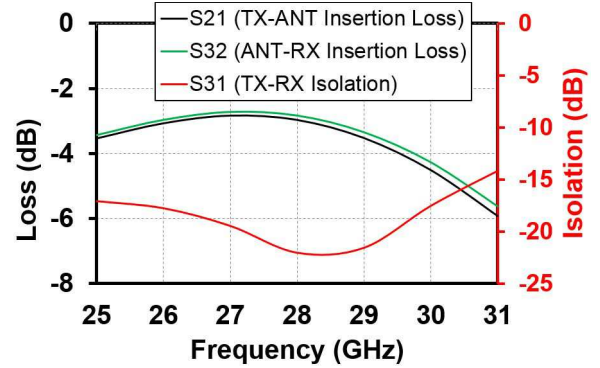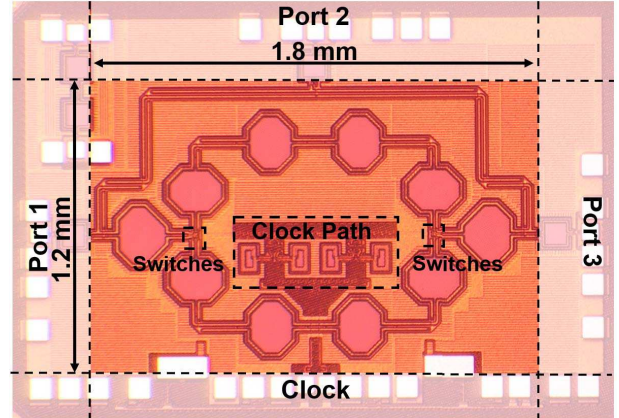Fig. 19. Circuit diagram of the quadrature modulation signal generation.

Fig. 20. Calculated transmission losses S_{21} and S_{32}.

Fig. 21. Postlayout simulations results of transmission losses S_{21} and S_{32} and isolation S_{31} of the 25-GHz 45-nm SOI CMOS doubly balanced circulator.

Fig. 22. Die micrograph of the 25-GHz doubly balanced circulator implemented in the GF 45-nm SOI CMOS process.

the switches. Independently controlled nMOS varactors at the differential LO inputs provide I/Q calibration of range $\pm 10°$. Interested readers can refer to [42] for more comprehensive implementation details.

B. Comparison Between Theory and Simulations

For this 25-GHz circulator, as mentioned earlier, Q_1 and Q_2 at 25 GHz are 15 each as the $\lambda/4$ sections were implemented using coplanar waveguides, and Q_3 at 25 GHz is 20 as it was implemented using C–L–C sections. Q_{sw} is 5.77 as the single-ended port impedance is 50 Ω and R_{sw} is 8.66 Ω. The quality factor of the delay line in the gyrator, Q_{NR} at 25 GHz, is 17. The Bragg frequency is 76 GHz, and the bandwidth of the modulation signal $0.35/t_r$ is 46.66 GHz. Hence, the modulation signals are limited to their fifth harmonics, as the intermodulation terms are formed. k_{filter} can therefore be calculated as shown in the following:

$$k_{filter}e^{-j\omega t} = \frac{-4}{\pi^2}\left[(-e^{j(\omega+\omega_m-\omega_m)t} - e^{j(\omega-\omega_m+\omega_m)t})\right.$$
$$+ \frac{1}{3^2}(-e^{j(\omega+3\omega_m-3\omega_m)t} - e^{j(\omega-3\omega_m+3\omega_m)t})$$
$$+ \left.\frac{1}{5^2}(-e^{j(\omega+5\omega_m-5\omega_m)t} - e^{j(\omega-5\omega_m+5\omega_m)t})\right]$$
$$= 0.933. \tag{51}$$

From (51), Q_{filter} can be calculated to be 28.9. Similarly, $(k_{Q_{NR}})_{truncated}$ can be calculated as shown in the following:

$$(k_{Q_{NR}})_{truncated}e^{-j\omega t}$$
$$= \frac{-4}{\pi^2}\left[\left(-e^{-\frac{3\pi}{4Q_{NR}}\sqrt{\frac{\omega+\omega_m}{\omega_m}}}e^{j(\omega+\omega_m-\omega_m)t}\right.\right.$$
$$\left.-e^{-\frac{3\pi}{4Q_{NR}}\sqrt{\frac{|\omega-\omega_m|}{\omega_m}}}e^{j(\omega-\omega_m+\omega_m)t}\right)$$
$$+\frac{1}{3^2}\left(-e^{-\frac{3\pi}{4Q_{NR}}\sqrt{\frac{\omega+3\omega_m}{\omega_m}}}e^{j(\omega+3\omega_m-3\omega_m)t}\right.$$
$$\left.-e^{-\frac{3\pi}{4Q_{NR}}\sqrt{\frac{|\omega-3\omega_m|}{\omega_m}}}e^{j(\omega-3\omega_m+3\omega_m)t}\right)$$
$$+\frac{1}{5^2}\left(-e^{-\frac{3\pi}{4Q_{NR}}\sqrt{\frac{\omega+5\omega_m}{\omega_m}}}e^{j(\omega+5\omega_m-5\omega_m)t}\right.$$
$$\left.\left.-e^{-\frac{3\pi}{4Q_{NR}}\sqrt{\frac{|\omega-5\omega_m|}{\omega_m}}}e^{j(\omega-5\omega_m+5\omega_m)t}\right)\right]$$
$$= 0.817. \tag{52}$$

From (52), $k_{Q_{NR}}$ can be calculated using $(k_{Q_{NR}})_{truncated}/k_{filter}$. Hence, $Q_{NR_{effec}}$ is 14.5. From (45) and (46), S_{21} and S_{32} are -2.66 dB each. Fig. 20 shows the distribution of circulator loss based the calculations from our analysis. The transmission losses, S_{21} and S_{32}, at center frequency from postlayout simulations assuming ideal baluns are -2.8 dB each, as shown in Fig. 21. Simulated transmission losses after deembedding the on-chip baluns are ≈ 3 dB. Therefore, the simulation results show close agreement with our analysis.

C. Measurements

The implemented circulator occupies an area of 1.2 mm $\times$ 1.8 mm, and Fig. 22 shows the die micrograph. The circulator was implemented with on-chip baluns for measurement purposes. The measurements were performed through RF probing in a chip-on-board configuration, and the
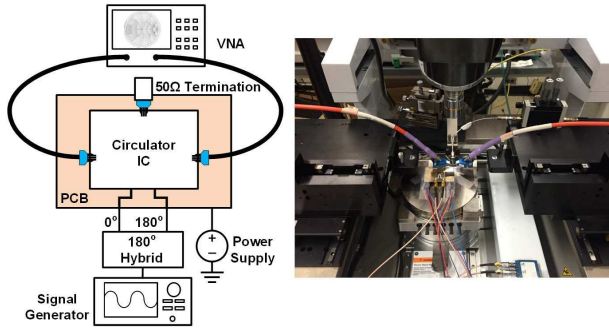
This article has been accepted for inclusion in a future issue of this journal. Content is final as presented, with the exception of pagination.

NAGULU *et al.*: NONRECIPROCAL COMPONENTS BASED ON SWITCHED TRANSMISSION LINES 17

Fig. 23. S-parameter measurement by probing two ports at a time, with a broadband 50-Ω millimeter-wave probe termination on the third port.

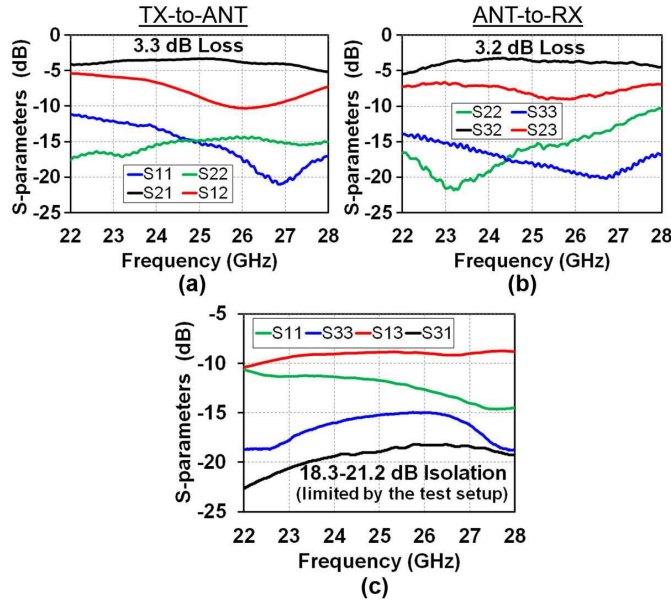Fig. 25. Measured TX–ANT group delay of the on-chip balun-circulator-balun structure.

Fig. 24. (a) Measured S-parameters between port 1 and port 2 when port 3 is terminated with a 50-Ω termination. (b) Measured S-parameters between port 2 and port 3 when port 1 is terminated with a 50-Ω termination. (c) Measured S-parameters between port 3 and port 1 when port 2 is terminated with a 50-Ω termination.

parameters in wireless applications. The group delay of the structure remains fairly constant within the signal bandwidth. As shown in Fig. 25, the group delay of the circulator varies <4% over a bandwidth of 2 GHz.

Importantly, the measured insertion losses are close to the postlayout simulations and the analytical calculations, validating the ability of the analysis presented in this paper to illuminate design tradeoffs and provide accurate estimates of performance. The measured isolation of 18.9 dB is limited by the measurement setup. For all circulators, if the ANT port is terminated with an imperfect impedance, the TX–RX isolation will be limited to the return loss at the ANT port. Here, the 18.9-dB isolation is limited by the reflection coefficient of the millimeter-wave probe and its broadband termination. In general, and at millimeter-wave frequencies in particular, an antenna tuner must be tightly integrated with the circulator to obtain the best TX–RX isolation.

VII. CONCLUSION

This paper presented various nonreciprocal structures, such as a frequency-conversion isolator, a broadband isolator, gyrators, a broadband circulator, and highly linear single-ended and differential circulators, enabled by using switch-based spatio-temporal conductivity modulation around transmission lines. The working principle of these structures has been explained using the time-domain analysis. In addition, we have also provided a detailed analysis for estimating the transmission losses by factoring in various nonidealities encountered during implementation. We have shown that the theoretically estimated loss matches closely with our simulation and measurement results. Such an analysis can aid the designer in choosing between different implementation technologies, fabrication processes, and nonreciprocal element topologies, and in optimizing performance by making better tradeoffs.

Topics for future research include the discovery of new topologies that further improve insertion loss, isolation bandwidth, and linearity, the incorporation of antenna tuning functionality into the circulator architecture, and the investigation and mitigation of the impact of clock phase noise on the circulator performance.

baluns are deembedded to obtain the circulator performance. A 180° hybrid (Krytar 4010265) is used to generate the differential (0°/180°) 8.33-GHz signals from a signal generator to drive the clock inputs of the circulator. A two-port Anritsu 37397E Lightning VNA is used to measure the S-parameters by probing two ports at a time, while a millimeter-wave probe terminated with a broadband 50-Ω termination is landed on the third port (see Fig. 23).

With the circulator configured for clockwise circulation with 8.33-GHz modulation signals, the measured transmissions in the clockwise direction S_{21}, S_{32} and S_{13}, shown in Fig. 24, are -3.3, -3.2, and -8.7 dB, respectively, without any port impedance tuning. The measured isolations in the reverse direction S_{12}, S_{23} and S_{31}, shown in Fig. 24, are 10.9, 9, and 18.9 dB, respectively, without any port impedance tuning. The design of the circulator was optimized to give the best performance for S_{21}, S_{32}, and S_{31} because these (TX–ANT loss, ANT–RX loss, and TX–RX isolation) are the most critical
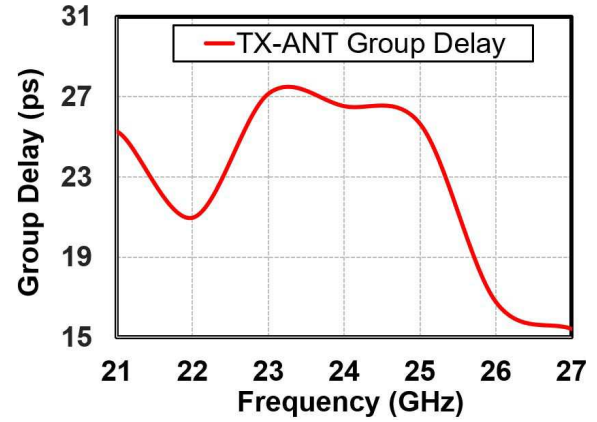
REFERENCES

[1] D. Bharadia, E. McMilin, and S. Katti, "Full duplex radios," *ACM SIGCOMM Comput. Commun. Rev.*, vol. 43, no. 4, pp. 375–386, Sep. 2013.

[2] A. Sabharwal, P. Schniter, D. Guo, D. W. Bliss, S. Rangarajan, and R. Wichman, "In-band full-duplex wireless: Challenges and opportunities," *IEEE J. Sel. Areas Commun.*, vol. 32, no. 9, pp. 1637–1652, Sep. 2014.

[3] B. Debaillie *et al.*, "Analog/RF solutions enabling compact full-duplex radios," *IEEE J. Sel. Areas Commun.*, vol. 32, no. 9, pp. 1662–1673, Sep. 2014.

[4] D. Yang, H. Yüksel, and A. Molnar, "A wideband highly integrated and widely tunable transceiver for in-band full-duplex communication," *IEEE J. Solid-State Circuits*, vol. 50, no. 5, pp. 1189–1202, May 2015.

[5] D.-J. van den Broek, E. A. M. Klumperink, and B. Nauta, "An in-band full-duplex radio receiver with a passive vector modulator downmixer for self-interference cancellation," *IEEE J. Solid-State Circuits*, vol. 50, no. 12, pp. 3003–3014, Dec. 2015.

[6] D. Korpi *et al.*, "Full-duplex mobile device: Pushing the limits," *IEEE Commun. Mag.*, vol. 54, no. 9, pp. 80–87, Sep. 2016.

[7] J. Zhou *et al.*, "Integrated full duplex radios," *IEEE Commun. Mag.*, vol. 55, no. 4, pp. 142–151, Apr. 2017.

[8] N. Reiskarimian, M. B. Dastjerdi, J. Zhou, and H. Krishnaswamy, "Highly-linear integrated magnetic-free circulator-receiver for full-duplex wireless," in *IEEE Int. Solid-State Circuits Conf. (ISSCC) Tech. Dig. Papers*, Feb. 2017, pp. 316–317.

[9] N. Reiskarimian, J. Zhou, and H. Krishnaswamy, "A CMOS passive LPTV nonmagnetic circulator and its application in a full-duplex receiver," *IEEE J. Solid-State Circuits*, vol. 52, no. 5, pp. 1358–1372, May 2017.

[10] M. B. Dastjerdi, N. Reiskarimian, T. Chen, G. Zussman, and H. Krishnaswamy, "Full duplex circulator-receiver phased array employing self-interference cancellation via beamforming," in *Proc. IEEE Radio Freq. Integr. Circuits Symp. (RFIC)*, Jun. 2018, pp. 1–4.

[11] B. D. H. Tellegen, "The gyrator, A new electric network element," *Philips Res. Rep.*, vol. 3, no. 81, pp. 3003–3014, Dec. 1948.

[12] H. J. Carlin, "On the physical realizability of linear non-reciprocal networks," *Proc. IRE*, vol. 43, no. 5, pp. 608–616, May 1955.

[13] R. Y. Barazarte, G. G. Gonzalez, and M. Ehsani, "Generalized gyrator theory," *IEEE Trans. Power Electron.*, vol. 25, no. 7, pp. 1832–1837, Jul. 2010.

[14] P. J. Allen, "The turnstile circulator," *IRE Trans. Microw. Theory Techn.*, vol. 4, no. 4, pp. 223–227, Oct. 1956.

[15] H. Bosma, "On stripline Y-circulation at UHF," *IEEE Trans. Microw. Theory Techn.*, vol. 12, no. 1, pp. 61–72, Jan. 1964.

[16] S. Tanaka, N. Shimomura, and K. Ohtake, "Active circulators—The realization of circulators using transistors," *Proc. IEEE*, vol. 53, no. 3, pp. 260–267, Mar. 1965.

[17] S. Wang, C.-H. Lee, and Y.-B. Wu, "Fully integrated 10-GHz active circulator and quasi-circulator using bridged-T networks in standard CMOS," *IEEE Trans. Very Large Scale Integr. (VLSI) Syst.*, vol. 24, no. 10, pp. 3184–3192, Oct. 2016.

[18] T. Kodera, D. L. Sounas, and C. Caloz, "Artificial Faraday rotation using a ring metamaterial structure without static magnetic field," *Appl. Phys. Lett.*, vol. 99, no. 3, p. 031114, 2011.

[19] T. Kodera, D. L. Sounas, and C. Caloz, "Magnetless nonreciprocal metamaterial (MNM) technology: Application to microwave components," *IEEE Trans. Microw. Theory Techn.*, vol. 61, no. 3, pp. 1030–1042, Mar. 2013.

[20] G. Carchon and B. Nauwelaers, "Power and noise limitations of active circulators," *IEEE Trans. Microw. Theory Techn.*, vol. 48, no. 2, pp. 316–319, Feb. 2000.

[21] B. Peng *et al.*, "Parity–time-symmetric whispering-gallery microcavities," *Nature Phys.*, vol. 10, pp. 394–398, Apr. 2014.

[22] L. Fan *et al.*, "An all-silicon passive optical diode," *Science*, vol. 335, pp. 447–450, Jan. 2012.

[23] K. Gallo, G. Assanto, K. R. Parameswaran, and M. M. Fejer, "All-optical diode in a periodically poled lithium niobate waveguide," *Appl. Phys. Lett.*, vol. 79, no. 3, pp. 314–316, 2001.

[24] A. M. Mahmoud, A. R. Davoyan, and N. Engheta, "All-passive nonreciprocal metastructure," *Nature Commun.*, vol. 6, Jul. 2015, Art. no. 8359.

[25] S. Qin, Q. Xu, and Y. E. Wang, "Nonreciprocal components with distributedly modulated capacitors," *IEEE Trans. Microw. Theory Techn.*, vol. 62, no. 10, pp. 2260–2272, Oct. 2014.

[26] N. A. Estep *et al.*, "Magnetic-free non-reciprocity and isolation based on parametrically modulated coupled-resonator loops," *Nature Phys.*, vol. 10, no. 12, pp. 923–927, Nov. 2014.

[27] N. A. Estep, D. L. Sounas, and A. Alù, "Magnetless microwave circulators based on spatiotemporally modulated rings of coupled resonators," *IEEE Trans. Microw. Theory Techn.*, vol. 64, no. 2, pp. 502–518, Feb. 2016.

[28] D. L. Sounas and A. Alù, "Non-reciprocal photonics based on time modulation," *Nature Photon.*, vol. 11, no. 12, pp. 774–783, Dec. 2017.

[29] S. Tyagi *et al.*, "An advanced low power, high performance, strained channel 65 nm technology," in *IEDM Tech. Dig.*, Dec. 2005, pp. 245–247.

[30] N. Reiskarimian and H. Krishnaswamy, "Magnetic-free non-reciprocity based on staggered commutation," *Nature Commun.*, vol. 7, Apr. 2016, Art. no. 11217.

[31] T. Dinc and H. Krishnaswamy, "A 28GHz magnetic-free non-reciprocal passive CMOS circulator based on spatio-temporal conductance modulation," in *IEEE Int. Solid-State Circuits Conf. (ISSCC) Tech. Dig. Papers*, Feb. 2017, pp. 294–295.

[32] T. Dinc, M. Tymchenko, A. Nagulu, D. Sounas, A. Alù, and H. Krishnaswamy, "Synchronized conductivity modulation to realize broadband lossless magnetic-free non-reciprocity," *Nature Commun.*, vol. 8, Oct. 2017, Art. no. 765.

[33] M. M. Biedka, R. Zhu, Q. M. Xu, and Y. E. Wang, "Ultra-wide band non-reciprocity through sequentially-switched delay lines," *Sci. Rep.*, vol. 7, Jan. 2017, Art. no. 40014.

[34] M. Biedka, Q. Wu, X. Zou, S. Qin, and Y. E. Wang, "Integrated time-varying electromagnetic devices for ultra-wide band nonreciprocity," in *Proc. IEEE Radio Wireless Symp. (RWS)*, Jan. 2018, pp. 80–83.

[35] J. Krol and S. Gong, "A non-magnetic gyrator utilizing switched delay lines," in *Proc. Eur. Microw. Conf. (EuMC)*, Oct. 2017, pp. 452–455.

[36] H. Krishnaswamy, A. Nagulu, N. Reiskarimian, and T. Dinc, "Integrated non-magnetic non-reciprocal components based on switch-based conductivity modulation," in *Proc. IEEE Int. Microw. RF Conf. (IMaRC)*, Dec. 2017.

[37] C. Andrews and A. C. Molnar, "A passive mixer-first receiver with digitally controlled and widely tunable RF interface," *IEEE J. Solid-State Circuits*, vol. 45, no. 12, pp. 2696–2708, Dec. 2010.

[38] A. Ghaffari, E. A. M. Klumperink, M. C. M. Soer, and B. Nauta, "Tunable high-Q N-path band-pass filters: Modeling and verification," *IEEE J. Solid-State Circuits*, vol. 46, no. 5, pp. 998–1010, May 2011.

[39] S. Hameed, M. Rachid, B. Daneshrad, and S. Pamarti, "Frequency-domain analysis of N-path filters using conversion matrices," *IEEE Trans. Circuits Syst. II, Exp. Briefs*, vol. 63, no. 1, pp. 74–78, Jan. 2016.

[40] S. Hameed, M. Rachid, B. Daneshrad, and S. Pamarti, "Frequency-domain analysis of a mixer-first receiver using conversion matrices," in *Proc. IEEE Int. Symp. Circuits Syst.*, May 2015, pp. 541–544.

[41] Q. Zhang, T. Guo, B. A. Khan, T. Kodera, and C. Caloz, "Coupling matrix synthesis of nonreciprocal lossless two-port networks using gyrators and inverters," *IEEE Trans. Microw. Theory Techn.*, vol. 63, no. 9, pp. 2782–2792, Sep. 2015.

[42] T. Dinc, A. Nagulu, and H. Krishnaswamy, "A millimeter-wave non-magnetic passive SOI CMOS circulator based on spatio-temporal conductivity modulation," *IEEE J. Solid-State Circuits*, vol. 52, no. 12, pp. 3276–3292, Dec. 2017.

Aravind Nagulu (S'17) received the B.Tech. and M.Tech. degrees in electrical engineering from IIT Madras, Chennai, India, in 2016. He is currently pursuing the Ph.D. degree in electrical engineering at Columbia University, New York, NY, USA. During his master's studies, he was involved in the implementation of a high-resolution continuous-time delta–sigma modulator.

His current research interests include exploring new directions to break reciprocity for emerging wireless communication paradigms and experimental validation of nonreciprocal analog/RF/millimeter-wave integrated circuits and systems.

Mr. Nagulu was a recipient of the IEEE RFIC Symposium Best Student Paper Award (First Place) in 2018.

Tolga Dinc (S'09) received the B.S. and M.S. degrees from Sabanci University, Istanbul, Turkey, in 2010 and 2012, respectively, and the Ph.D. degree from Columbia University, New York, NY, USA, in 2018, all in electrical engineering.

He is currently with Kilby Labs, Texas Instruments Incorporated, Dallas, TX, USA, as an RF/Millimeter-Wave Engineer. He has authored/co-authored over 30 peer-reviewed papers in the area of RF/mm-wave integrated circuits, antennas, and systems.

Dr. Tolga was a recipient of several honors and awards, including the Columbia EE Jury Award in 2017, the IEEE MTT-S Graduate Fellowship in 2016, the IEEE RFIC Symposium Best Student Paper Award (First Place) in 2015, the 2012 Sabanci University Gursel Sonmez Research Award, and the IEEE MTT-S Undergraduate/Pre-Graduate Scholarship Award in 2010.
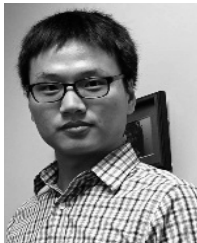
Zhicheng Xiao received the B.S. and M.Eng. degrees in applied physics and electrical engineering from Hunan University, Changsha, China, in 2009 and 2012, respectively, and the M.S. degree in electro-optics from the University of Dayton, Dayton, OH, USA, in 2014. He is currently pursuing the Ph.D. degree at the Department of Electrical and Computer Engineering, The University of Texas at Austin (UT Austin), Austin, TX, USA.

His current research interests include parity-time symmetry and magnetless nonreciprocity.

Mr. Xiao was a recipient of the 2015 Engineering School Fellowship at UT Austin and the 2017 URSI Travel Scholarship.

Mykhailo Tymchenko received the B.S. and M.S. degrees in theoretical physics from V. N. Karazin Kharkiv National University, Kharkiv, Ukraine, in 2009 and 2010, respectively. He is currently pursuing the Ph.D. degree at the Department of Electrical and Computer Engineering, The University of Texas at Austin, Austin, TX, USA.

He was a Visiting Scholar with the University of Zaragoza, Zaragoza, Spain, in 2012. He has authored or co-authored over 25 papers in top-tier journals and 1 book chapter. He holds two patents. His current research interests include linear and nonlinear metasurfaces, plasmonics, topological photonics, graphene, and magnetless nonreciprocal and time-periodic systems.

Mr. Tymchenko was a recipient of the University of Texas Graduate School Fellowship from 2013 to 2017.

Dimitrios L. Sounas (M'11–SM'17) received the Ph.D. degree (Hons.) in electrical and computer engineering from the Aristotle University of Salonica, Salonica, Greece, in 2009.

From 2010 to 2015, he was a Post-Doctoral Fellow with Polytechnique Montreal, Montreal, QC, Canada, and The University of Texas at Austin, Austin, TX, USA, where he has been a Research Scientist since 2015. In 2015, he joined the FOM Institute AMOLF, Amsterdam, The Netherlands, as a Visiting Researcher. His major contributions can be found in the area of magnetless nonreciprocal components and have attracted significant interest from the industry and the military for inclusion in the next-generation wireless communication systems. He has contributed to the founding of Silicon Audio RF Circulator, Austin, TX, USA, specializing in the design of angular-momentum circulators for RF and acoustical systems. He has authored or co-authored 63 journal papers, 113 conference papers, and 2 book chapters, and holds 4 patents, among which are papers published in highly selective journals, including *Science*, various *Nature* journals, various *Physical Review* journals, and the IEEE TRANSACTIONS. His current research interests include electromagnetics, plasmonics, optics, and acoustics, with a particular emphasis on the design of nonreciprocal, nonlinear, and active devices.

Dr. Sounas has chaired various sessions in international symposia and organized a special session about graphene devices during the EuCAP 2016 International Symposium. He has been a Reviewer for more than 20 engineering and physics journals.

Andrea Alù (S'03–M'07–SM'12–F'14) received the Laurea, M.S., and Ph.D. degrees from the University of Roma Tre, Rome, Italy, in 2001, 2003, and 2007, respectively.

From 2002 to 2008, he was with the University of Pennsylvania, Philadelphia, PA, USA, where he has also developed significant parts of his Ph.D. and postgraduate research. He was a Post-Doctoral Research Fellow with the University of Pennsylvania, Philadelphia, PA, USA, for one year. In 2009, he joined the faculty of The University of Texas at Austin, Austin, TX, USA, where he was the Temple Foundation Endowed Professor until 2018 and is currently an Adjunct Professor, a Senior Research Scientist, and a member of the Wireless Networking and Communications Group. He is the Founding Director of the Photonics Initiative, Advanced Science Research Center, Graduate Center of the City University of New York, New York, NY, USA, where he is also the Einstein Professor of physics with the Graduate Center and a Professor of electrical engineering with the City College of New York. He co-authored a book on optical antennas and has authored or co-authored over 400 journal papers and over 30 book chapters, with over 20 000 citations to date. His current research interests include metamaterials and plasmonics, electromangetics, optics and nanophotonics, acoustics, scattering, nanocircuits and nanostructures, miniaturized antennas and nanoantennas, and RF antennas and circuits.

Dr. Alù is a full member of URSI and a Fellow of the OSA, SPIE, and APS. Over the last few years, he was the recipient of several research awards, including the ICO Prize in Optics in 2016, the Inaugural MDPI Materials Young Investigator Award in 2016, the Kavli Foundation Early Career Lectureship in Materials Science in 2016, the Inaugural ACS Photonics Young Investigator Award Lectureship in 2016, the Edith and Peter O'Donnell Award in Engineering in 2016, the NSF Alan T. Waterman Award in 2015, the IEEE MTT-S Outstanding Young Engineer Award in 2014, the OSA Adolph Lomb Medal in 2013, the IUPAP Young Scientist Prize in Optics in 2013, the Franco Strazzabosco Award for Young Engineers in 2013, the SPIE Early Career Investigator Award in 2012, the URSI Issac Koga Gold Medal in 2011, the NSF CAREER Award in 2010, the AFOSR and the DTRA Young Investigator Award in 2010 and 2011, and the Young Scientist Award from the URSI General Assembly in 2005 and the URSI Commission B in 2010, 2007, and 2004, respectively. His students have been the recipients of several awards, including Student Paper Awards of the IEEE Antennas and Propagation Symposia (in 2011 to Y. Zhao and in 2012 to J. Soric). He has been a Simons Investigator in Physics since 2016, has been selected three times as a Finalist of the Blavatnik Award for Young Scientists in 2016, 2017, and 2018, and is a 2017 Highly Cited Researcher from Web of Science. He has been serving as an OSA Traveling Lecturer since 2010 and the IEEE AP-S Distinguished Lecturer since 2014. He has been serving on the IEEE Joint AP-S and MTT-S Chapter for Central Texas. He has organized and chaired various special sessions in international symposia and conferences and was the Technical Program Chair for the IEEE AP-S Symposium in 2016 and for the International Metamaterials Conference in 2014 and 2015. He served as an Associate Editor for the IEEE ANTENNAS AND WIRELESS PROPAGATION LETTERS, *Scientific Reports*, *Metamaterials*, *Advanced Electromagnetics*, and *Optics Express*. He has guest edited special issues for the IEEE JOURNAL OF SELECTED TOPICS IN QUANTUM ELECTRONICS, the IEEE ANTENNAS AND WIRELESS PROPAGATION LETTERS, *Nanophotonics*, the *Journal of Optics*, the *Journal of the Optical Society of America B*, *Photonics and Nanostructures: Fundamentals and Applications*, *Optics Communications*, *Metamaterials*, and *Sensors* on a variety of topics involving metamaterials, plasmonics, optics, and electromagnetic theory. He is currently on the Editorial Board of *Physical Review B*, *New Journal of Physics*, *Advanced Optical Materials*, *Materials* (MDPI), *EPJ Applied Metamaterials*, and *Metamaterials* (ISTE).

Harish Krishnaswamy (S'03–M'09) received the B.Tech. degree in electrical engineering from IIT Madras, Chennai, India, in 2001, and the M.S. and Ph.D. degrees in electrical engineering from the University of Southern California (USC), Los Angeles, CA, USA, in 2003 and 2009, respectively.

In 2009, he joined the Electrical Engineering Department, Columbia University, New York, NY, USA, where he is currently an Associate Professor and the Director of the Columbia High-Speed and Millimeter-Wave IC Laboratory (CoSMIC). In 2017, he co-founded MixComm Inc., a venture-backed startup, to commercialize CoSMIC Laboratory's advanced wireless research. His current research interests include integrated devices, circuits, and systems for a variety of RF, mm-wave, and sub-mm-wave applications.

Dr. Krishnaswamy has been a member of the Technical Program Committee of several conferences, including the IEEE International Solid-State Circuits Conference since 2015 and the IEEE Radio Frequency Integrated Circuits Symposium since 2013. He was a recipient of the IEEE International Solid-State Circuits Conference Lewis Winner Award for Outstanding Paper in 2007, the Best Thesis in Experimental Research Award from the USC Viterbi School of Engineering in 2009, the Defense Advanced Research Projects Agency Young Faculty Award in 2011, the 2014 IBM Faculty Award, the Best Demo Award at the 2017 IEEE ISSCC, and the Best Student Paper Awards (First Place) at the 2015 and 2018 IEEE Radio Frequency Integrated Circuits Symposium. He currently serves as a Distinguished Lecturer for the IEEE Solid-State Circuits Society and a member of the DARPA Microelectronics Exploratory Council.